Microstructure and Creep Properties of Dispersion-Strengthened Aluminum Alloys

J. RÖSLER, R. JOOS, and E. ARZT

The mechanical properties of dispersion-strengthened aluminum alloys, with various dispersoid types, volume fractions, and grain structures, were investigated in conjunction with systematic microstructural examinations. New theoretical concepts, based on thermally activated dislocation detachment from dispersoid particles, were used to analyze the creep behavior. A particularly strong dispersoid-dislocation interaction was identified as reason for the excellent creep properties of carbide dispersion-strengthened aluminum. Oxide particles (Al_2O_3, MgO) seem to exert a weaker interaction force and are therefore less efficient strengtheners. Although fine crystalline in the as-extruded condition, all alloys are remarkably resistant against diffusional creep. It is demonstrated that this behavior can be consistently understood by extending the concept developed for the interaction between bulk dislocations and dispersoids to grain boundary dislocations.

I. INTRODUCTION

DISPERSION strengthening is a promising means of extending the temperature capability of aluminum alloys far beyond the limits of conventional precipitation-hardened alloys. This concept originated in a discovery made by Irmann,[1] who found that, compared to cast aluminum, hot-pressed aluminum powders had a substantially higher hardness which was retained even after annealing at temperatures up to 773 K.[1,2] The extraordinary high-temperature properties of this material, subsequently known as "SAP" (Sintered-Aluminum-Powder), led to intensive investigations in the 1950s and 1960s (for a review, see Reference 3). Its commercial breakthrough, however, was hampered mainly for processing-related reasons: the inhomogeneous distribution of relatively coarse dispersoid particles, which severely impaired ductility,[4] and material blistering due to hydrogen formation at high temperatures. The advent of new processing techniques in the 1970s, notably high-energy ball milling[5] and reaction milling,[6,7] has made it possible to overcome these weaknesses. A much finer dispersoid distribution can now be achieved, which leads to a better balance between strength and ductility. It is this progress, combined with an increased need for lightweight high-temperature materials, which has triggered renewed interest in this material class.[8,9,10]

The present article deals with the high-temperature creep behavior of advanced dispersion-strengthened aluminum alloys produced by reaction milling. The creep properties have been investigated in the temperature range between 573 and 773 K in both compression and tension. In order to study the interrelation between creep strength and microstructure, materials with different dispersoid particles (aluminum oxide, aluminum carbide, and magnesium oxide), dispersoid volume fractions (ranging from 2 to 10 vol pct), and grain structures (grain sizes between submicron and millimeters) were investigated.

In the as-received condition, dispersion-strengthened aluminum alloys generally exhibit very small grain sizes ($d \leq 2\ \mu m$), and it can therefore be expected that the creep strength is basically controlled by (1) the strengthening effect of the dispersoid particles and (2) the onset of diffusional creep, which can adversely affect the creep properties. Both contributions have to be considered for high-temperature applications. Recent developments in the theory of dispersion strengthening, which will be briefly reviewed, suggest that the strengthening contribution from dispersoid particles depends sensitively on the properties of the particle-matrix interface. This means that dispersoids of the same size and volume fraction but of different crystal structure may affect the creep strength in different ways. Since the interface properties are a function of both dispersoid structure and matrix material, suitable dispersoids have to be found separately for each material class. An attempt will be made here to identify those particles for aluminum matrices. It will be demonstrated that significant improvements in creep strength are likely by optimizing the type of dispersoid with regard to the interface properties.

In fine-grained materials, the creep strength will ultimately be limited by diffusional creep. Therefore, we have employed secondary recrystallization to produce an extremely coarse and elongated grain structure in addition to the fine-grained structure of the as-received materials. It will be shown that the gain in high-temperature strength is less than might be expected from comparison with other dispersion-strengthened materials but can be significant at very high temperatures and small strain rates. Comparison between the two materials reveals some remarkable interactions between dispersion strengthening and diffusional creep processes, which will be discussed on the basis of present theoretical models.

This article first describes the experimental details (Section II), then the results of the microstructural and mechanical property investigations (Section III). A theoretical interpretation of our findings is given in

J. RÖSLER, formerly Project Group Leader, Max-Planck-Institut für Metallforschung, is Project Leader, Asea Brown Boveri Ltd., ABB Corporate Research, CH-5405 Baden, Switzerland. R. JOOS, University Assistant, is with the University of Stuttgart. E. ARZT, Professor and Director, is with the University of Stuttgart and Max-Planck-Institut für Metallforschung, respectively, D-7000 Stuttgart, Federal Republic of Germany.

Manuscript submitted February 1, 1991.

Section IV. The symbols used throughout the article are listed in Table I.

II. EXPERIMENTAL

A. *As-Received Materials*

Materials studied in this investigation were supplied by Sintermetallwerk Krebsöge (Radevormwald, Germany) and Erbslöh Aluminum (Velbert, Germany) in the form of extruded rods with a diameter of 12 mm. The fabrication process included reaction milling[6,7] of gas-atomized powders under controlled addition of carbon and subsequent consolidation by cold compaction and hot extrusion (extrusion ratio $\approx$ 20:1, $T \approx$ 823 K). The chemical composition of the as-received materials was analyzed with respect to Mg, C, and O (Table II). The materials referred to as AlC0, AlC1, and AlC2 consist of pure aluminum matrices and 0, 1, and 2 wt pct carbon, respectively. Alloy AlMg4C1 contains the same amount of carbon as AlC1 but was produced by using an aluminum powder prealloyed with 4 wt pct Mg. Calculated dispersoid volume fractions are also listed in Table II. Compression and tension test specimens were machined from the extruded rods parallel and perpendicular to the extrusion axis. Cylindrical samples with dimensions of 6 by 12 mm were used for compression testing. The cylindrical tensile specimens had a cross section of 6 mm and a gage length of 40 mm.[11]

Table I. Nomenclature

G	shear modulus
E	elastic modulus
$\mathbf{b}$	lattice Burgers vector
$\mathbf{b}_{gb}$	Burgers vector of grain boundary dislocations
Ω	atomic volume
$k_B T$	thermal energy
M	Taylor factor
σ	normal stress
$\sigma_{0.2}$	yield stress
σ_g, σ_O	strengthening contribution due to Hall-Petch and Orowan strengthening, respectively
σ_d	athermal detachment stress
σ_{th}^l, σ_{th}^g	"threshold" stress for local and general climb, respectively
$\dot{\varepsilon}$	strain rate
n	stress exponent
δD_b	grain boundary diffusion coefficient
$a_p D_p$	pipe diffusion coefficient
D_v	volume diffusion coefficient
D_{eff}	effective diffusion coefficient $D_{\text{eff}} = D_v \cdot (1 + \pi\delta D_b/(d_g D_v))$
ρ	dislocation density
ρ_{gb}^e	density of grain boundary edge dislocations
2λ	interparticle spacing
T_M, T_P	dislocation line energy in the matrix and at a particle, respectively
k	relaxation factor
GAR	grain aspect ratio
d_g	grain size
d_p, r	particle diameter and radius, respectively
γ_{gb}	specific grain boundary energy
f_v, f_v^{gb}	volume fraction of particles in the bulk and at grain boundaries

B. *Recrystallization*

In order to study the influence of grain size on the mechanical properties, material AlC0 was recrystallized to an extremely coarse grain structure of high aspect ratio.[12] No temperature gradient had to be applied during thermal treatment in order to obtain grain elongation in extrusion direction (Section III–A–1). Best results were obtained by a two-stage process: (1) cold swaging of the as-received material from 12- to 6-mm diameter and heat treatment at 573 to 673 K for about 1 hour; (2) cold swaging to 5-mm diameter and heat treatment for 20 minutes at 873 K. Prior to testing, complete recrystallization was ensured by inspection under polarized light. For that purpose, specimens were polished and electrolytically etched with a solution of 0.7 g H_3BO_3, 10 ml HF (40 pct), and 200 ml H_2O.[13]

Materials other than AlC0 could not be recrystallized even after severe thermomechanical processing (cold swaging to 3-mm diameter and heat treatment at 873 K/100 hours), presumably because the Zener back stress[14] exceeds the driving force for grain growth at higher particle volume fractions. In its recrystallized form, AlC0 will be referred throughout this article as AlC0R. Smaller specimen diameters (compression, 4.5 mm; tension, 3 mm in gage section) had to be chosen for this material because of the reduction in cross section during thermomechanical treatment.

C. *Mechanical Testing*

Constant strain-rate compression creep tests were performed at 573, 673, and 773 K on a Schenck-Trebel RMC 100 electromechanical testing machine. The specimens were induction heated, with an axial temperature gradient in the gage section of less than 2 K at all temperatures. A function generator was used in conjunction with a high-temperature extensometer to keep the strain rate constant during the test. The load was monitored as a function of time and converted into true stress, taking

Table II. Chemical Composition (in Weight Percent) and Calculated Dispersoid Volume Fraction f_v (in Volume Percent) of the Alloys Investigated*

Alloy	Al	Mg	C	O	$f_v^{Al_4C_3}$	$f_v^{Al_2O_3}$	f_v^{MgO}	f_v^{total}
AlC0	bulk	—	0.031	0.98	0.11	1.75	—	1.86
AlC1	bulk	—	1.24	0.78	4.57	1.40	—	5.97
AlMg4C1	bulk	3.95	1.42	2.57	5.24	—	4.91	10.15
AlC2	bulk	—	2.16	0.80	7.97	1.43	—	9.40

*The dispersoid volume fractions have been calculated with the following density values: $\rho_{Al_4C_3} = 2.93$ g/cm^3,[24] $\rho_{Al_2O_3} = 4.2$ g/cm^3,[22] and $\rho_{MgO} = 4.58$ g/cm^3.[48] It was assumed that carbon and oxygen transformed quantitatively to stable carbides and oxides during hot extrusion.

the shape change of the specimen into account. For a complete description of the test apparatus, see Reference 11. The compression tests were stopped after reaching strains of typically 5 pct. Steady-state creep, as exhibited by a constant creep stress, was achieved after less than 2 pct deformation and prevailed throughout the test. After testing, the specimens were cooled under constant load to retain the dislocation structure. In the majority of tests, the stress axis was oriented parallel to the extrusion direction. For material AlC0, compressive tests were also run in the transverse direction.

Tensile creep tests were performed at the same temperatures in a screw-driven Roell-Korthaus DSM 6100F creep tester under constant load. The specimens were heated in an air furnace, and the axial strain was recorded. The steady-state strain rate was obtained from a representation of strain *vs* time and is reported subsequently. Tests were typically run until fracture of the specimen.

The specimen dimensions used for compression and tension testing are specified in Sections A and B for the as-received and recrystallized materials, respectively. The tensile samples of the recrystallized material contained typically 40 to 50 grains per gage cross section.

D. *Transmission Electron Microscopy*

Longitudinal and transverse sections were cut from the specimens and ground to a thickness of about 150 μm. Discs with 3-mm diameter were then electropolished in a 33 pct HNO_3-67 pct CH_3OH solution at about 243 K. Voltages of 30 to 35 V were found to give the best results. Transmission electron microscope (TEM) investigations were performed in a JEOL 200CX microscope at 200 kV with energy-dispersive X-ray (EDX) facilities.

III. RESULTS

A. *Microstructural Examination*

1. *Grain structure*

The grain size of the as-extruded alloys (Figures 1 through 3) is in the submicron range, which is typical of mechanically milled aluminum alloys.[15,16] Table III lists the mean linear intercept grain size d_g in a plane perpendicular to the extrusion axis. It varies inversely with the particle volume fraction f_v, which is indicative of grain growth controlled by the Zener mechanism.[14] The Zener grain size estimated by $d_g^z \approx d_p/f_v$ (d_p is particle diameter) is in reasonable agreement with the measured values (Table III).

That the grain structure is controlled by the dispersoid particles is also demonstrated by the apparent grain elongation in extrusion direction (Figures 1(b), 2(b), and 3(a)), which is especially pronounced in the case of material AlC0 (Figure 2(b)), containing only oxide dispersoids. The stringers of oxide particles, visible in Figure 2(b), obviously restrict grain growth in the transverse direction. Their origin seems closely related to oxide films on prior powder particle surfaces, which were broken up incompletely during milling and then extended longitudinally during hot extrusion. Interestingly, the formation of dispersoid stringers is less pronounced at higher carbon contents (compare Figures 1(b), 2(b), and 3(a)), which

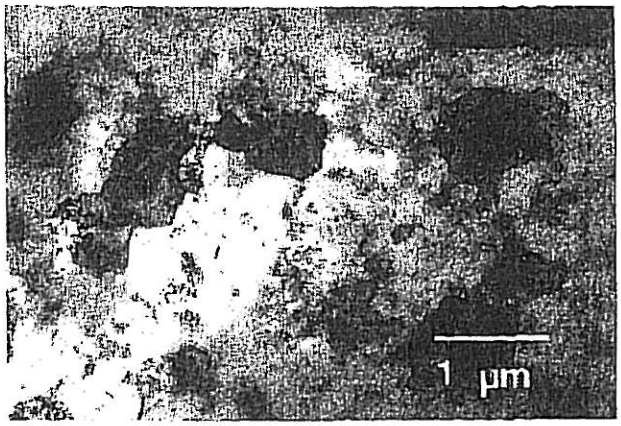

(*a*)

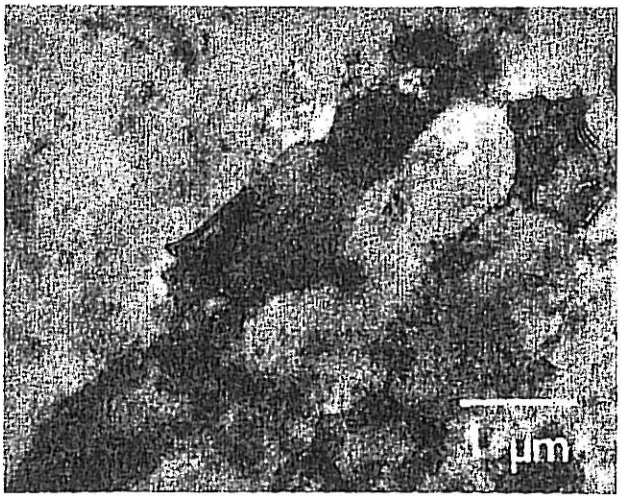

(*b*)

Fig. 1—Microstructure of alloy AlC2 in (*a*) transverse and (*b*) longitudinal section.

may be due to the beneficial effect of carbon as a lubricant during powder milling. The more homogeneous particle distribution is also accompanied by a more equiaxed grain structure (Figures 1(b), 2(b), and 3(a) and Table III).

It is noteworthy that the elongated grains of alloy AlC0 are frequently divided into smaller entities by transverse subgrain boundaries, which are composed of lattice dislocations. To a lesser extent, these subgrain boundaries where also observed in alloy AlC1 (Figures 3(a) and (b)) but could hardly be detected in alloys AlC2 and AlMg4C1.

The grain structure of all materials was remarkably stable during thermal treatment. No significant grain coarsening could be detected after annealing at 773 K for 100 hours. Also, thermomechanical treatment (Section II–B) was not capable of altering the grain structure of alloys AlMg4C1, AlC2, and AlC1, where the grain boundaries are too firmly locked by the high volume fraction of thermally stable dispersoids. Alloy AlC0, by contrast, could be recrystallized to an extremely coarse-grained microstructure (Figure 4). Grains

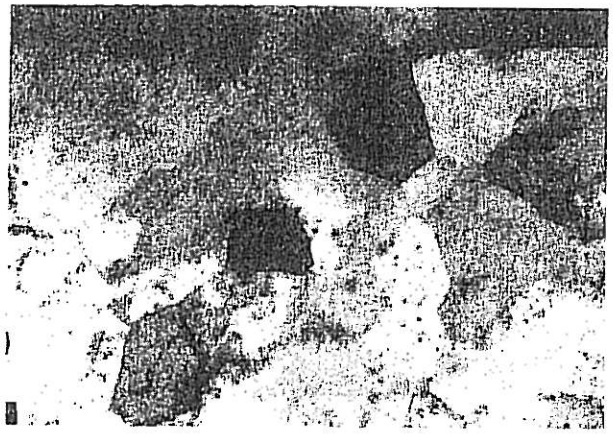

(*a*)

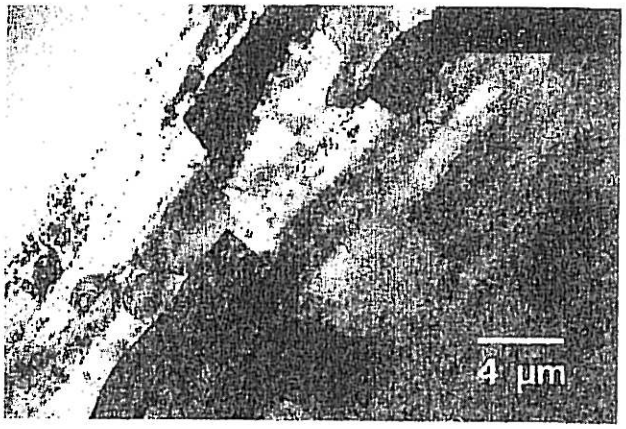

(*b*)

Fig. 2—Microstructure of alloy AlC0 in (*a*) transverse and (*b*) longitudinal section. The columnar grains and dispersoid rows are oriented in extrusion direction.

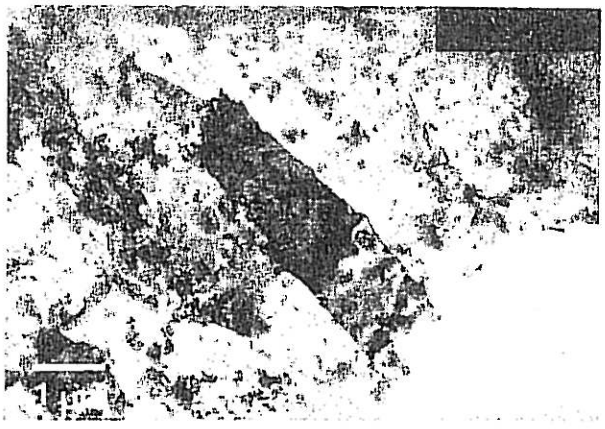

(*a*)

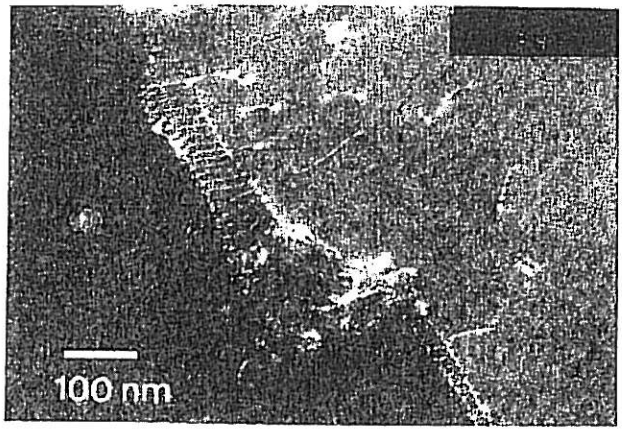

(*b*)

Fig. 3—Microstructure of alloy AlC1 (longitudinal section). The center area of (a) is magnified in (b), showing a subboundary which divides a strongly elongated grain.

are strongly elongated after this treatment. The mean linear intercept grain sizes perpendicular and parallel to the extrusion axis are 330 and 5000 μm, respectively. Again, the high grain aspect ratio (GAR) is probably a consequence of the aligned dispersoid distribution.

2. *Texture*

Besides their different grain structures, alloys AlC0 and AlC0R exhibit different textures as well. In the as-received condition, an extremely strong ⟨111⟩ fiber texture with a much weaker ⟨100⟩ side component is found (Figures 5(a) through (c)), which is typical of extruded aluminum.[17] Accordingly, the Taylor factor is close to $M_{111} = 3.66$. We take $M = 3.6$ for this material.

Due to the large grain size, the texture of the recrystallized material is more difficult to determine. However, it is evident from inspection of Figure 5 that the

Table III. List of Mean Intercept Grain Sizes (d_g) Measured in a Plane Perpendicular to the Extrusion Axis, Grain Aspect Ratios (GAR), and Zener Grain Sizes (d_g^z) (Section III–A–1) for Materials Investigated

Alloy	d_g [μm]	d_g^z [μm]	GAR
AlC0R	330	—	15
AlC0	1.9	1.6	2.1
AlC1	1.2	0.7	1.8
AlMg4C1	0.4	0.3	1.6
AlC2	0.7	0.5	1.6

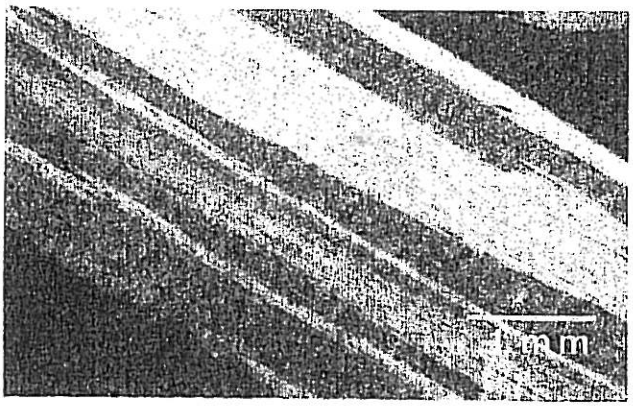

Fig. 4—Microstructure of the recrystallized alloy AlC0R (longitudinal section). The grains are extremely coarse and strongly elongated in extrusion direction.

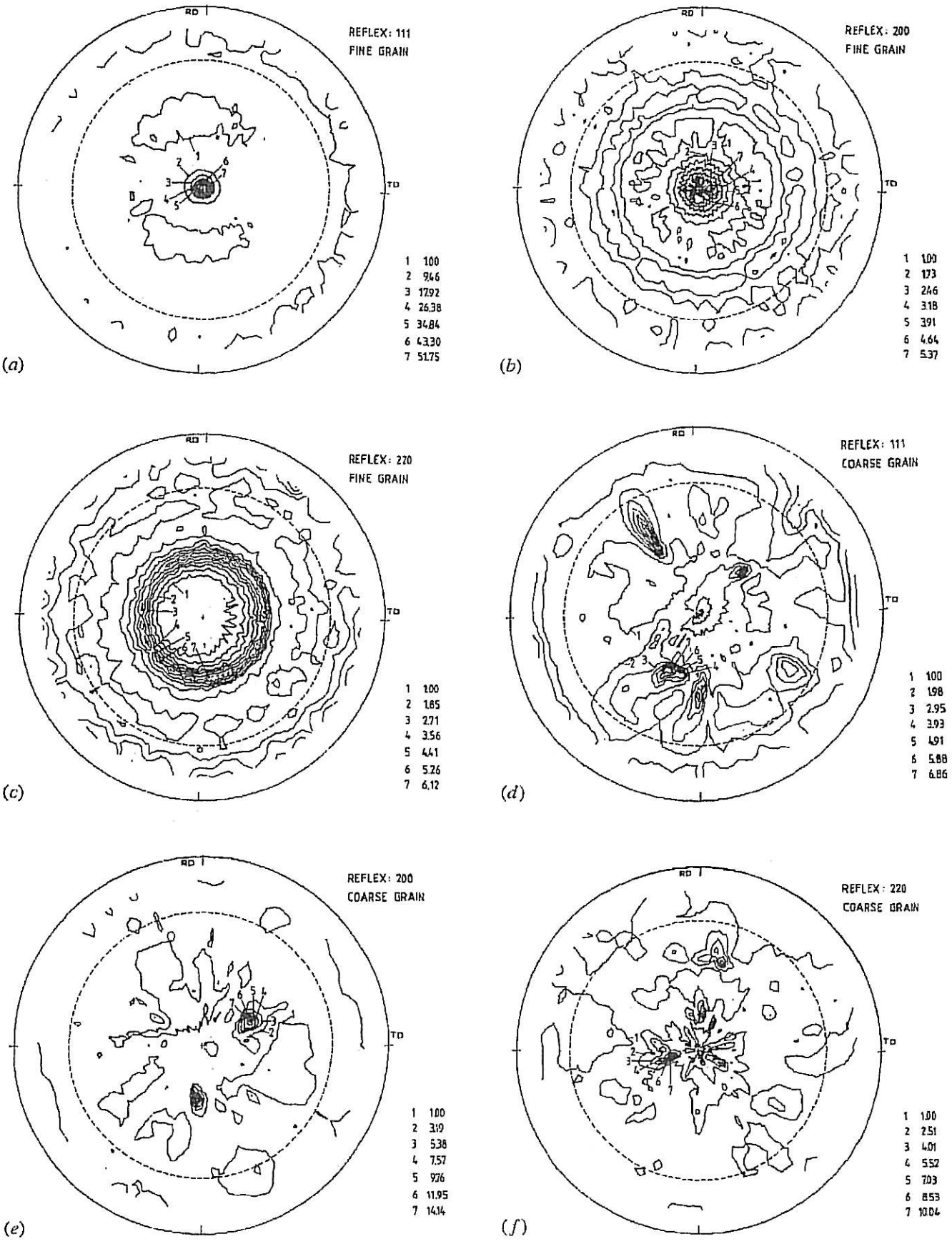

Fig. 5—⟨111⟩, ⟨200⟩, and ⟨220⟩ pole figures for materials (*a*) through (*c*) AlC0 and (*d*) through (*f*) AlC0R. The extrusion axis is oriented parallel to the X-ray beam. Also indicated are intensities as multiples of the mean value.

extrusion texture has vanished. Apart from a slightly higher ⟨220⟩ intensity in extrusion direction, no strong preference of a particular crystallographic direction is found. Thus, we assume $M = 3.3$ for material AlC0R, which is intermediate between the value for a statistical distribution and $M_{220} = 3.66$.

Although texture measurements have not been undertaken for the other fine-grained materials, it seems safe to assume an extrusion texture similar to that of AlC0. A value of $M = 3.6$ was therefore taken for these materials as well.

3. *Second-phase particles*

a. *Aluminum oxide*

During powder milling, aluminum hydroxide films form spontaneously on freshly exposed metal surfaces and are incorporated in the metal by consecutive welding and fracturing of the powder particles.[18] These hydroxides, which are known to be amorphous,[19] crystallize during heat treatment above $T \approx 723$ K.[15,20,21] Which crystallographic modification is formed depends upon the nature of the amorphous hydroxide and the annealing temperature. According to Gitzen,[22] χ- γ-, η-, and α-Al_2O_3 are most likely to form at the annealing and consolidation temperatures used here ($T \approx 823$ K). However, transformation temperatures can be substantially lowered in contact with metallic aluminum,[20] so that the formation of the high-temperature modifications κ-, δ-, and θ-Al_2O_3 cannot be ruled out completely.

Figure 6 shows a diffraction pattern of alloy AlC0. The finely distributed oxide particles, which constitute the only second phase in this material, give rise to three intense Debye-Scherrer rings, as indicated. The corresponding lattice spacings have been determined as $d_1 = 0.239$ nm, $d_2 = 0.197$ nm, and $d_3 = 0.140$ nm. The ring diameters were measured to an accuracy of ± 0.1 mm with a glass ruler, and the camera length of the TEM was calibrated using aluminum matrix reflections. This reduces the error margin in determining the lattice spacing to approximately 1 pct.[11] In Table IV, the three most intense reflections of all possible Al_2O_3 modifications are given. Comparing the experimental results with the data of Table IV, no correspondence is found within the error margin for α-, χ-, κ-, δ-, and θ-Al_2O_3. Instead, the observed pattern fits the most intense reflections of γ- and η-Al_2O_3. To distinguish between these two modifications, a quantitative knowledge of the observed intensities would be necessary. Both oxides form a spinel-type lattice,[22,23] in which the oxygen atoms occupy the anion places of the spinel lattice and

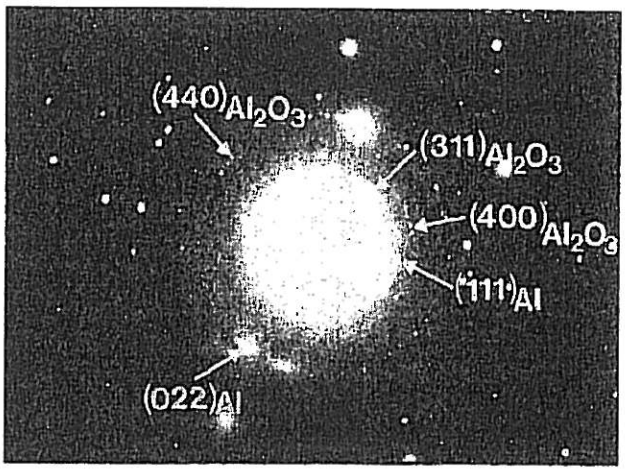

Fig. 6—Electron diffraction pattern of alloy AlC0. Three Debye Scherrer rings are visible which correspond to γ- or η-Al_2O_3. The (111)- und (022)-Al reflections are also indicated.

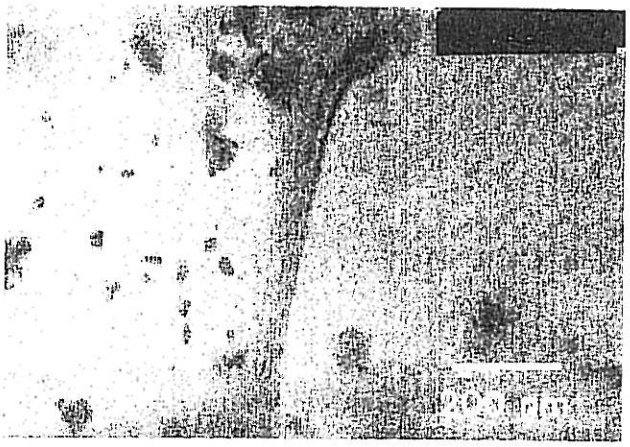

Fig. 7—TEM micrograph of alloy AlC0 (transverse section). The Al_2O_3 dispersoids are roughly equiaxed in shape.

Table IV. Diffraction Data for Possible Al_2O_3 Modifications*

α-Al_2O_3			χ-Al_2O_3			γ-Al_2O_3			η-Al_2O_3		
d (Å)	I/I_{max}	(hkl)	d (Å)	I/I_{max}	(hkl)	d (Å)	I/I_{max}	(hkl)	d (Å)	I/I_{max}	(hkl)
2.552	90	104	2.41	50	200	2.39	80	311	2.40	60	311
2.085	100	113	2.12	50	202	1.977	100	400	1.97	80	400
1.601	80	116	1.395	100	220	1.395	100	440	1.40	100	440
κ-Al_2O_3			δ-Al_2O_3			Θ-Al_2O_3					
d (Å)	I/I_{max}	(hkl)	d (Å)	I/I_{max}	(hkl)	d (Å)	I/I_{max}	(hkl)			
2.57	80	—	2.73	80	—	2.85	80	004			
2.11	80	—	1.99	80	—	2.72	80	200			
1.39	100	—	1.39	100	—	1.39	100	$12\bar{2}$, 215			

*The lattice spacings d, Miller indices (hkl), and relative diffraction intensities I/I_{max} for the three most intensive reflections of each modification are listed.

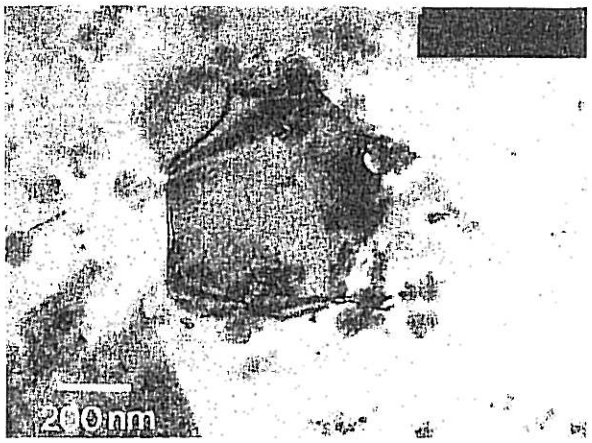

(*a*)

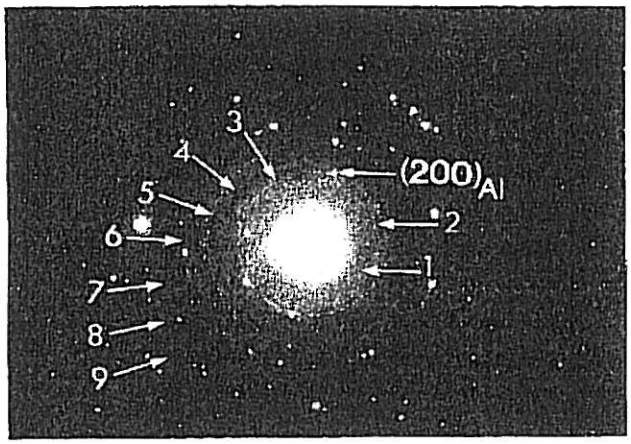

(*b*)

Fig. 8—(*a*) TEM micrograph and (*b*) diffraction pattern of alloy AlMg4C1. The Debye-Scherrer pattern, which corresponds to the finely distributed second-phase particles, is numbered in accordance with Table V. A (200) diffraction spot of the aluminum matrix is also indicated.

the 21 1/3 Al atoms per unit cell are statistically distributed over the 24 cation places. The lattice parameters are $a = 0.795$ nm and $a = 0.790$ nm for γ- and η-Al_2O_3, respectively.[22]

Compared to the platelike morphology of the aluminum-carbide particles (Section III–A–3–c), the oxide particles are roughly equiaxed in shape (Figure 7). From the measurement of more than 600 particles, a typical particle diameter of 30 nm was found.

b. *Magnesium oxide*

Due to the high affinity of magnesium for oxygen, aluminum oxide may be replaced by magnesium oxide in the magnesium containing alloy AlMg4C1. The microstructure and diffraction pattern of this material are shown in Figures 8(a) and (b). The corresponding lattice spacings of the Debye-Scherrer pattern visible in Figure 8(b) are listed in Table V. Comparison with Table IV shows that the (311)-, (400)-, and (440)-Al_2O_3 reflections are in fact no longer detectable. To distinguish between MgO and the spinel $MgAl_2O_4$, the diffraction data are compared with the experimental data in Table V. In the case of $MgAl_2O_4$, a strong (202) reflection would be expected but is not found experimentally. Instead, the data correspond well to MgO, also with respect to relative intensities. The (200) reflection is most intense, followed by the (220) reflection, while the (400) reflection is very weak. Note that reflections 1 and 4 in Figure 8(b) correspond to the carbide Al_4C_3, as discussed below.

The substitution of Al_2O_3 by MgO appears to be quantitative, because the diffraction pattern of the aluminum oxide has disappeared completely. Simple calculation shows that 3.9 wt pct Mg is required to dissipate the oxygen content of 2.57 wt pct (Table II) by the formation of MgO. Thus, practically no magnesium seems to stay in solid solution, and alloy AlMg4C1 has therefore to be regarded as an essentially pure aluminum matrix—similar to alloys AlC0, AlC1, and AlC2—dispersion strengthened by MgO and Al_4C_3 particles. Further evidence that Mg is no longer in solid solution comes from EDX measurements: magnesium could only be detected in the MgO particles but not in the bulk material (Figure 9).

Table V. Comparison of Experimentally Measured Lattice Spacings d_{exp} (Column 2) and Intensities I (Column 3, Qualitative) with the Diffraction Data for MgO and $MgAl_2O_4$ According to the ASTM Tables (Column 4 through 9)*

Reflex Number	d_{exp} (Å)	I	MgO			$MgAl_2O_4$			Indexation
			d (Å)	I/I_{max}	hkl	d (Å)	I/I_{max}	hkl	
—	—	—	—	—	—	3.155	80	202	—
1	2.81	—	—	—	—	—	—	—	(012)-Al_4C_3
2	2.43	w	2.431	10	111	2.428	20	302	(111)-MgO
3	2.11	s	2.106	100	200	2.103	100	303	(200)-MgO
4	1.67	—	—	—	—	—	—	—	(110)-Al_4C_3
5	1.48	m	1.489	52	220	1.481	30	413	(220)-MgO
6	1.21	w	1.216	12	222	1.215	10	700	(222)-MgO
7	1.05	vw	1.053	5	400	—	—	—	(400)-MgO
8	0.94	w	0.942	17	420	—	—	—	(420)-MgO
9	0.86	w	0.860	15	422	—	—	—	(422)-MgO

*Final indexation in column 10 as discussed in text. The numbering in column 1 corresponds to that in Fig. 8(b). s = strong; m = medium; w = weak; vw = very weak.

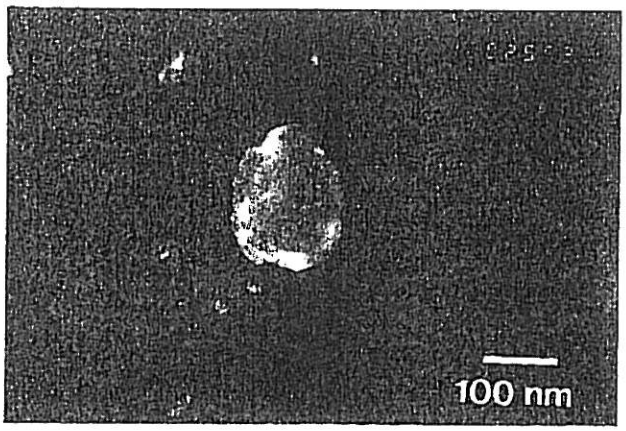

Fig. 9—Dark-field TEM micrograph showing a MgO particle. Magnesium could only be detected at the location of the particle.

The typical particle diameter in alloy AlMg4C1 was determined to be about 34 nm from the measurement of more than 200 particles, which included MgO as well as Al_4C_3 particles. The platelike geometry of the Al_4C_3 particles (see below) has been taken into account only in a simple way, by determining the diameter of a sphere with equal projected area. The value given above is therefore only a rough approximation.

c. *Aluminum carbide*

Next, alloys milled under addition of carbon were investigated. Carbon, which is finely distributed within the matrix during powder milling, reacts to Al_4C_3 after heat treatment. A diffraction pattern of alloy AlC2 (Figure 10) shows two diffraction rings corresponding to lattice spacings $d_1 = 0.280$ nm and $d_2 = 0.167$ nm. They can be identified as $d_{012} = 0.280$ nm and $d_{110} = 0.166$ nm Al_4C_3 reflections which, according to the ASTM tables, are the most intense ones.

Since alloys AlC1, AlMg4C1, and AlC2 contain oxide particles as well, the morphology of the carbides cannot be determined directly from bright-field TEM micrographs. Numerous dark-field images, as well as lattice imaging, (Figures 11(a) through (c)) reveal a platelike

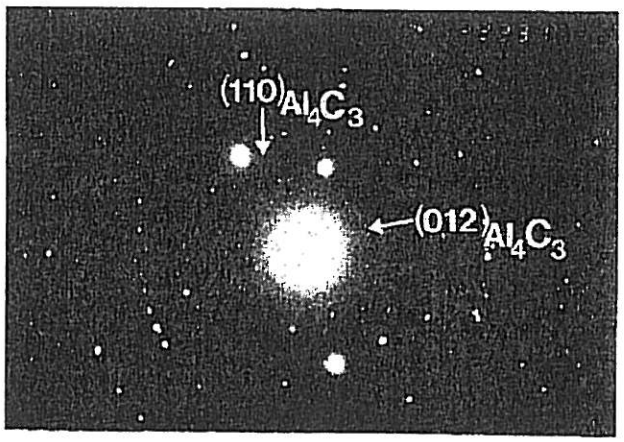

Fig. 10—Diffraction pattern of alloy AlC2. The $(110)_{Al_4C_3}$ and $(012)_{Al_4C_3}$ reflections are identified.

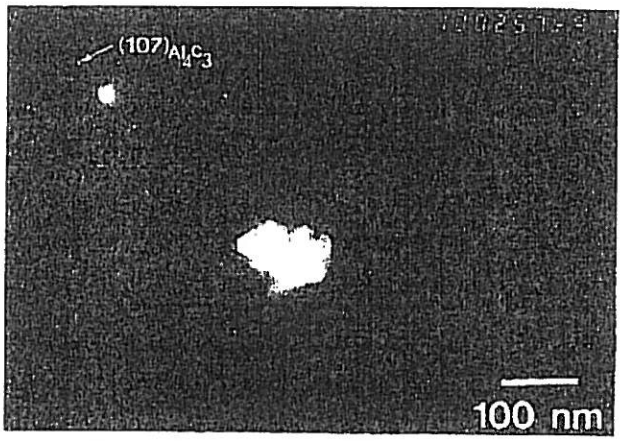

(*a*)

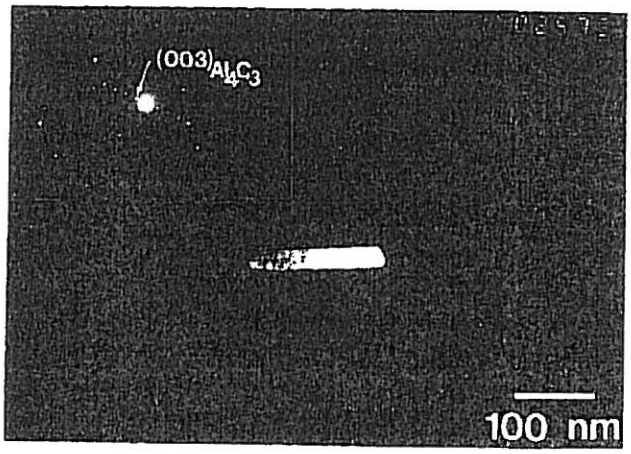

(*b*)

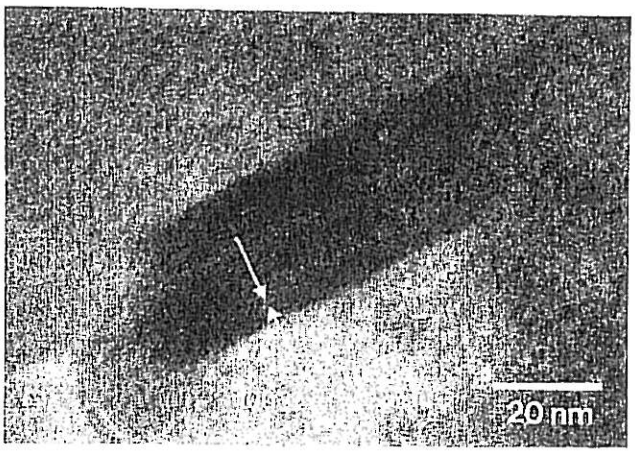

(*c*)

Fig. 11—Dark-field imaging of an Al_4C_3 particle at two different orientations relative to the electron beam (*a*) imaging with the $(107)_{Al_4C_3}$ reflection, (*b*) imaging with the $(003)_{Al_4C_3}$ reflection, and (*c*) high-resolution imaging at the same orientation as in (b).

particle shape with the [003] direction as plate normal. According to Stackelberg and Schnorrenberg,[24] the Al_4C_3 crystal consists of alternating carbon and aluminum layers perpendicular to the [003] direction. Typically, growth

along directions involving alternating planes of different atom species is slow.[25] The platelike morphology of the Al_4C_3 dispersoids may therefore be caused by the preferential growth of the particles perpendicular to the [003] direction.

From the measurement of more than 500 particles, the overall particle size (carbides plus oxides) was determined to be $d = 41$ nm and $d = 43$ nm for alloys AlC1 and AlC2, respectively. The same limitations to the accuracy of the measurement as stated above apply.

B. *Mechanical Behavior*

1. *Room-temperature properties*

The values of the room-temperature yield strength $\sigma_{0.2}$ measured in tension are listed in Table VI. Neglecting the Peierls stress and noting that the dislocation density after hot extrusion is low (Figure 1(a)), the only strengthening mechanisms of significance are grain size hardening $\Delta\sigma_g$ and Orowan strengthening $\Delta\sigma_O$.

The value of $\Delta\sigma_g$ can be estimated by comparison of materials AlC0 and AlC0R. Correcting for the different Taylor factors M in both materials (Section 2), one finds that grain refinement increases the room-temperature strength by about 23 MPa. Equating the volume $\pi/4 \cdot d_g^3 \cdot \mathrm{GAR}$ of the roughly cylindrical grains with that of a spherical grain, an effective grain size $d_g' = d_g \cdot (1.5 \cdot \mathrm{GAR})^{1/3}$ is obtained, and the Hall-Petch constant $k_{HP} = \Delta\sigma_g \cdot (d_g')^{1/2}$ can be estimated as 0.038 MPa $\cdot$ m$^{1/2}$; this result compares well with values reported by Hansen.[26] Using this constant, $\Delta\sigma_g$ can be calculated for all other alloys (Table VI). It is noted that $\Delta\sigma_g$ is generally small compared to $\sigma_{0.2}$. Apparently, the strengthening contribution $\Delta\sigma_O = \sigma_{0.2} - \Delta\sigma_g$ of the dispersoid particles predominates even at room temperature.

The estimate of $\Delta\sigma_O$ can be cross-checked, noting that the Orowan stress is related to the particle diameters by

$$\Delta\sigma_O = 0.84 \cdot \frac{M}{2\pi\sqrt{1-\nu}} \cdot \frac{Gb}{d_p} \cdot \sqrt{\frac{6f_v}{\pi}} \cdot \ln\left(\frac{d_p}{2b}\right) \quad [1]$$

assuming a monosize particle distribution. Satisfactory correspondence is found (Table VI) by inserting values for d_p as given in Section 3 and f_v from Table II. In the case of materials AlC0 and AlC0R, the slight overestimation of $\Delta\sigma_O$ by Eq. [1] is, in fact, reasonable, considering the high particle concentration at the grain boundaries (Figure 2(b)), which reduces the "effective" volume fraction in the bulk material.

2. *High-temperature properties*

a. *Deformation*

The steady-state compression creep data are compiled in Table VII and plotted in normalized form, log $(\dot{\varepsilon}/D)$ *vs* log (σ/E), in Figures 12(a) through (e). A common feature of all creep data is a region of extremely high stress exponent ($n > 50$) at intermediate strain rates ($10^7\ \mathrm{m}^{-2} < \dot{\varepsilon}/D < 10^{11}\ \mathrm{m}^{-2}$). This high stress sensitivity is especially pronounced for the carbide dispersion-strengthened materials AlC1 and AlC2, where the creep strength is virtually independent of $\dot{\varepsilon}$ over four orders of magnitude. The TEM micrographs, taken after creep deformation, suggest that the rate-controlling deformation mechanism is the interaction of single dislocations with dispersoid particles. Dislocations are always found to be trapped at dispersoids (Figure 13(a)).

Whereas the region of high stress exponent extends to the lowest strain rates in the case of the coarse-grained material AlC0R (Figure 12(a)), the fine-grained alloys exhibit a transition to a lower stress exponent of about $n = 13$. Under transverse loading, where the grain elongation is perpendicular to the stress axis, $n = 13$ prevails, in fact, at all strain rates (Figure 12(b)).

At high creep rates ($\dot{\varepsilon}/D > 10^{11}\ \mathrm{m}^{-2}$), the stress exponent decreases as well. This is expected, because otherwise, the creep rate of the dispersion-strengthened material would eventually exceed that of the dispersion-free matrix material at high stresses (see schematic in Figure 14). Note that the particle-free matrix may undergo power-law breakdown at stresses necessary to deform its dispersion-hardened counterpart. Consequently, the stress exponent of the dispersion-strengthened material may stay relatively high ($n \gg 3$ to 5), although the deformation mechanism becomes "matrixlike." Transmission electron microscope micrographs confirm that the creep deformation at high strain rates is indeed no longer controlled by the interaction of single dislocations with particles. Instead, dislocation networks stabilized by larger dispersoid agglomerates are predominant (Figure 13(b)). Similar dislocation structures are typical of particle-free class II materials.

The results of tensile creep tests, which were performed for alloys AlC0 and AlC0R, are superimposed on the compression creep data in Figures 12(a) and (b) and listed in Table VIII. Similar stress-strain rate dependencies as under compressive stress are found.

b. *Fracture*

The strain at failure ε_f is plotted *vs* log $(\dot{\varepsilon})$ in Figure 15 for AlC0 and AlC0R. Notably, the fracture

Table VI. Compilation of the Room-Temperature Yield Strength $\sigma_{0.2}$ for the Different Alloys*

Material	$\sigma_{0.2}$ (MPa)	$\Delta\sigma_g$ (MPa)	$\Delta\sigma_O$ (MPa)	$\Delta\sigma_O^*$ (MPa)
AlC0R	82	0	82	105
AlC0	112	23	89	114
AlC1	180	29	151	161
AlC2	258	39	219	194
AlMg4C1	382	53	329	242

*Also listed are the estimates for grain size strengthening $\Delta\sigma_g$ and Orowan strengthening $\Delta\sigma_O$. $\Delta\sigma_O^*$ represents the Orowan contribution according to Eq. [1].

Table VII. Steady-State Compression Creep Data for Materials Investigated*

Material	T (K)	σ (MPa)	$\sigma/E \cdot 10^3$	$\dot{\varepsilon}$ (s^{-1})	$\dot{\varepsilon}/D_v$ (m^{-2})
AlC0	573	72.0	1.170	$1.0 \cdot 10^{-3}$	$5.18 \cdot 10^{13}$
		64.6	1.050	$1.0 \cdot 10^{-4}$	$5.18 \cdot 10^{12}$
		60.0	0.974	$3.1 \cdot 10^{-5}$	$1.61 \cdot 10^{12}$
		56.8	0.922	$1.0 \cdot 10^{-5}$	$5.18 \cdot 10^{11}$
		52.8	0.857	$1.0 \cdot 10^{-6}$	$5.18 \cdot 10^{10}$
		51.3	0.833	$1.0 \cdot 10^{-7}$	$5.18 \cdot 10^{9}$
	673	51.1	0.905	$1.0 \cdot 10^{-3}$	$6.18 \cdot 10^{11}$
		48.8	0.865	$5.1 \cdot 10^{-4}$	$3.15 \cdot 10^{11}$
		46.1	0.818	$1.0 \cdot 10^{-4}$	$6.18 \cdot 10^{10}$
		43.7	0.775	$3.3 \cdot 10^{-5}$	$2.04 \cdot 10^{10}$
		44.6	0.791	$1.3 \cdot 10^{-5}$	$8.04 \cdot 10^{9}$
		40.7	0.721	$1.0 \cdot 10^{-6}$	$6.18 \cdot 10^{8}$
		39.4	0.698	$1.0 \cdot 10^{-7}$	$6.18 \cdot 10^{7}$
	773	35.8	0.716	$1.0 \cdot 10^{-3}$	$2.32 \cdot 10^{10}$
		32.6	0.652	$3.1 \cdot 10^{-4}$	$7.19 \cdot 10^{9}$
		31.3	0.626	$1.0 \cdot 10^{-4}$	$2.32 \cdot 10^{9}$
		30.1	0.602	$1.0 \cdot 10^{-5}$	$2.32 \cdot 10^{8}$
		28.4	0.567	$1.0 \cdot 10^{-6}$	$2.32 \cdot 10^{7}$
		25.0	0.500	$1.0 \cdot 10^{-7}$	$2.32 \cdot 10^{6}$
	773	23.8	0.476	$1.0 \cdot 10^{-3}$	$2.32 \cdot 10^{10}$
	(transverse loading)	22.0	0.440	$4.9 \cdot 10^{-4}$	$1.14 \cdot 10^{10}$
		19.5	0.390	$1.0 \cdot 10^{-4}$	$2.32 \cdot 10^{9}$
		19.5	0.390	$5.8 \cdot 10^{-5}$	$1.35 \cdot 10^{9}$
		15.9	0.318	$9.7 \cdot 10^{-6}$	$2.25 \cdot 10^{8}$
		14.7	0.294	$6.5 \cdot 10^{-6}$	$1.51 \cdot 10^{8}$
		14.5	0.290	$9.5 \cdot 10^{-7}$	$2.20 \cdot 10^{7}$
		13.0	0.260	$7.2 \cdot 10^{-7}$	$1.67 \cdot 10^{7}$
AlC0R	773	33.0	0.660	$1.0 \cdot 10^{-3}$	$2.32 \cdot 10^{10}$
		33.4	0.668	$1.0 \cdot 10^{-3}$	$2.32 \cdot 10^{10}$
		31.2	0.624	$2.0 \cdot 10^{-4}$	$4.64 \cdot 10^{9}$
		31.5	0.630	$1.0 \cdot 10^{-4}$	$2.32 \cdot 10^{9}$
		31.9	0.638	$1.0 \cdot 10^{-4}$	$2.32 \cdot 10^{9}$
		30.4	0.608	$3.0 \cdot 10^{-5}$	$6.96 \cdot 10^{8}$
		31.2	0.624	$1.0 \cdot 10^{-5}$	$2.32 \cdot 10^{8}$
		29.6	0.592	$3.0 \cdot 10^{-6}$	$6.96 \cdot 10^{7}$
		30.0	0.600	$1.4 \cdot 10^{-6}$	$3.25 \cdot 10^{7}$
		27.9	0.558	$4.7 \cdot 10^{-7}$	$1.09 \cdot 10^{7}$
		30.8	0.616	$2.0 \cdot 10^{-7}$	$4.64 \cdot 10^{6}$
AlC1	573	109.1	1.77	$1.0 \cdot 10^{-3}$	$5.18 \cdot 10^{13}$
		92.6	1.50	$1.0 \cdot 10^{-4}$	$5.18 \cdot 10^{12}$
		81.4	1.32	$1.0 \cdot 10^{-5}$	$5.18 \cdot 10^{11}$
		76.4	1.24	$2.5 \cdot 10^{-6}$	$1.30 \cdot 10^{11}$
		76.7	1.24	$1.0 \cdot 10^{-6}$	$5.18 \cdot 10^{10}$
		76.9	1.25	$1.0 \cdot 10^{-7}$	$5.18 \cdot 10^{9}$
		77.0	1.25	$5.0 \cdot 10^{-8}$	$2.59 \cdot 10^{9}$
	673	69.4	1.23	$1.0 \cdot 10^{-3}$	$6.18 \cdot 10^{11}$
		60.8	1.08	$3.1 \cdot 10^{-4}$	$1.92 \cdot 10^{11}$
		62.0	1.10	$1.0 \cdot 10^{-4}$	$6.18 \cdot 10^{10}$
		60.8	1.08	$1.5 \cdot 10^{-5}$	$9.28 \cdot 10^{9}$
		62.2	1.10	$1.0 \cdot 10^{-5}$	$6.18 \cdot 10^{9}$
		62.9	1.12	$1.0 \cdot 10^{-6}$	$6.18 \cdot 10^{8}$
		62.7	1.11	$1.0 \cdot 10^{-7}$	$6.18 \cdot 10^{7}$
	773	43.6	0.873	$1.0 \cdot 10^{-3}$	$2.32 \cdot 10^{10}$
		42.0	0.840	$1.0 \cdot 10^{-4}$	$2.32 \cdot 10^{9}$
		40.1	0.803	$1.0 \cdot 10^{-5}$	$2.32 \cdot 10^{8}$
		38.7	0.775	$1.0 \cdot 10^{-6}$	$2.32 \cdot 10^{7}$
		38.1	0.761	$1.0 \cdot 10^{-7}$	$2.32 \cdot 10^{6}$
AlC2	573	168	2.73	$5.3 \cdot 10^{-3}$	$2.75 \cdot 10^{14}$
		161	2.61	$2.3 \cdot 10^{-3}$	$1.19 \cdot 10^{14}$
		147	2.39	$1.0 \cdot 10^{-3}$	$5.18 \cdot 10^{13}$

Table VII Cont. Steady-State Compression Creep Data for Materials Investigated*

Material	T (K)	σ (MPa)	$\sigma/E \cdot 10^3$	$\dot{\varepsilon}$ (s^{-1})	$\dot{\varepsilon}/D_v$ (m^{-2})
		146	2.37	$5.6 \cdot 10^{-4}$	$2.90 \cdot 10^{13}$
		132	2.14	$2.0 \cdot 10^{-4}$	$1.04 \cdot 10^{13}$
		129	2.09	$6.4 \cdot 10^{-5}$	$3.32 \cdot 10^{12}$
		122	1.98	$1.0 \cdot 10^{-5}$	$5.18 \cdot 10^{11}$
		121	1.96	$1.6 \cdot 10^{-6}$	$8.29 \cdot 10^{10}$
		118	1.92	$4.5 \cdot 10^{-7}$	$2.33 \cdot 10^{10}$
	673	104	1.84	$5.4 \cdot 10^{-3}$	$3.34 \cdot 10^{12}$
		97	1.72	$1.0 \cdot 10^{-3}$	$6.18 \cdot 10^{11}$
		97	1.72	$6.5 \cdot 10^{-4}$	$4.02 \cdot 10^{11}$
		96	1.70	$5.9 \cdot 10^{-4}$	$3.65 \cdot 10^{11}$
		94	1.67	$5.5 \cdot 10^{-4}$	$3.40 \cdot 10^{11}$
		103	1.83	$5.2 \cdot 10^{-5}$	$3.22 \cdot 10^{10}$
		99	1.76	$2.5 \cdot 10^{-6}$	$1.55 \cdot 10^{9}$
		102	1.81	$2.4 \cdot 10^{-6}$	$1.48 \cdot 10^{9}$
		96	1.70	$4.3 \cdot 10^{-7}$	$2.66 \cdot 10^{8}$
		98	1.74	$1.0 \cdot 10^{-7}$	$6.18 \cdot 10^{7}$
	773	71	1.42	$2.6 \cdot 10^{-3}$	$6.03 \cdot 10^{10}$
		69	1.38	$6.1 \cdot 10^{-4}$	$1.41 \cdot 10^{10}$
		76	1.52	$1.0 \cdot 10^{-4}$	$2.32 \cdot 10^{9}$
		70	1.40	$6.0 \cdot 10^{-5}$	$1.39 \cdot 10^{9}$
		70	1.40	$5.9 \cdot 10^{-5}$	$1.37 \cdot 10^{9}$
		71	1.42	$7.5 \cdot 10^{-6}$	$1.74 \cdot 10^{8}$
		69	1.38	$1.0 \cdot 10^{-6}$	$2.32 \cdot 10^{7}$
		66	1.32	$5.0 \cdot 10^{-7}$	$1.16 \cdot 10^{7}$
		68	1.36	$3.0 \cdot 10^{-7}$	$6.96 \cdot 10^{6}$
		63	1.26	$1.0 \cdot 10^{-7}$	$2.32 \cdot 10^{6}$
		52	1.04	$3.1 \cdot 10^{-8}$	$7.19 \cdot 10^{5}$
AlMg4C1	573	128.7	2.09	$1.1 \cdot 10^{-3}$	$5.70 \cdot 10^{13}$
		122.4	1.98	$1.0 \cdot 10^{-4}$	$5.18 \cdot 10^{12}$
		121.1	1.97	$5.1 \cdot 10^{-5}$	$2.64 \cdot 10^{12}$
		116.7	1.89	$2.1 \cdot 10^{-5}$	$1.09 \cdot 10^{12}$
		116.7	1.89	$1.0 \cdot 10^{-5}$	$5.18 \cdot 10^{11}$
		115.6	1.88	$5.1 \cdot 10^{-6}$	$2.64 \cdot 10^{11}$
		115.6	1.88	$1.0 \cdot 10^{-6}$	$5.18 \cdot 10^{10}$
		114.5	1.86	$5.1 \cdot 10^{-7}$	$2.64 \cdot 10^{10}$
		111.3	1.81	$1.0 \cdot 10^{-7}$	$5.18 \cdot 10^{9}$
	673	89.6	1.59	$5.0 \cdot 10^{-3}$	$3.09 \cdot 10^{12}$
		84.7	1.50	$1.0 \cdot 10^{-3}$	$6.18 \cdot 10^{11}$
		84.0	1.49	$1.0 \cdot 10^{-4}$	$6.18 \cdot 10^{10}$
		85.0	1.51	$1.0 \cdot 10^{-4}$	$6.18 \cdot 10^{10}$
		83.0	1.47	$5.1 \cdot 10^{-5}$	$3.15 \cdot 10^{10}$
		84.0	1.49	$5.1 \cdot 10^{-5}$	$3.15 \cdot 10^{10}$
		83.0	1.47	$2.1 \cdot 10^{-5}$	$1.30 \cdot 10^{10}$
		83.0	1.47	$2.1 \cdot 10^{-5}$	$1.30 \cdot 10^{10}$
		78.0	1.38	$1.0 \cdot 10^{-5}$	$6.18 \cdot 10^{9}$
		81.0	1.44	$5.1 \cdot 10^{-6}$	$3.15 \cdot 10^{9}$
		78.0	1.38	$1.0 \cdot 10^{-6}$	$6.18 \cdot 10^{8}$
		76.0	1.35	$5.1 \cdot 10^{-7}$	$3.15 \cdot 10^{8}$
		67.9	1.20	$2.5 \cdot 10^{-7}$	$1.55 \cdot 10^{8}$
		66.0	1.17	$1.0 \cdot 10^{-7}$	$6.18 \cdot 10^{7}$
	773	48.0	0.96	$1.0 \cdot 10^{-4}$	$2.32 \cdot 10^{9}$
		43.6	0.87	$5.1 \cdot 10^{-5}$	$1.18 \cdot 10^{9}$
		41.5	0.83	$1.0 \cdot 10^{-5}$	$2.32 \cdot 10^{8}$
		39.3	0.79	$5.1 \cdot 10^{-6}$	$1.18 \cdot 10^{8}$
		38.2	0.76	$1.8 \cdot 10^{-6}$	$4.18 \cdot 10^{7}$
		36.0	0.72	$1.0 \cdot 10^{-6}$	$2.32 \cdot 10^{7}$
		34.9	0.70	$5.2 \cdot 10^{-7}$	$1.21 \cdot 10^{7}$
		29.5	0.59	$1.0 \cdot 10^{-7}$	$2.32 \cdot 10^{6}$

*The loading direction is parallel to the extrusion axis unless otherwise stated. Data for the elastic modulus and the diffusion coefficient have been obtained from References 49 and 50, respectively.

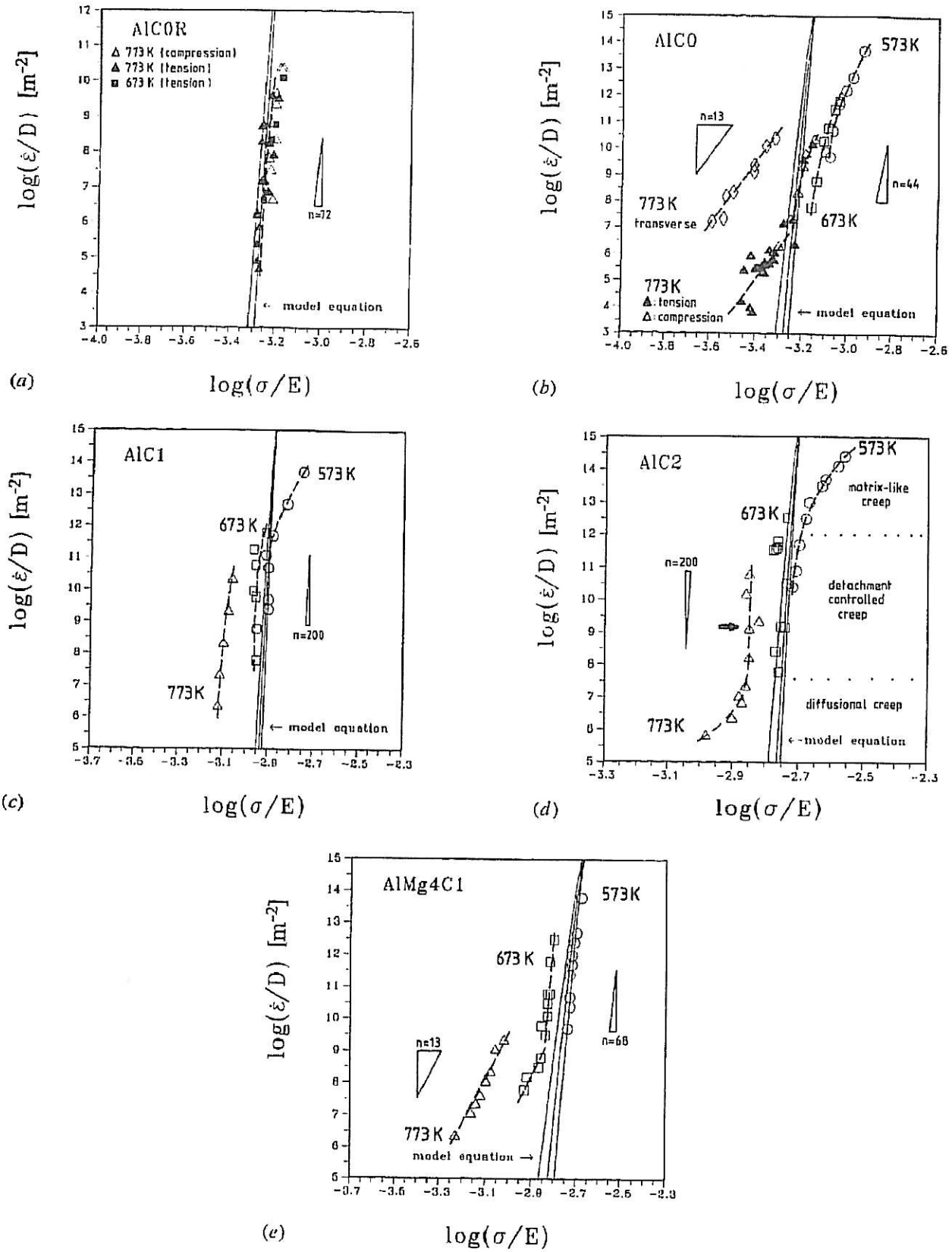

Fig. 12—Steady-state creep data plotted in normalized form $\dot{\varepsilon}/D_v$ *vs* σ/E. The stress axis is parallel to the extrusion direction unless otherwise stated. Open and full symbols represent compression and tension creep results, respectively. Solid lines represent the theoretical stress-strain dependence for detachment-controlled dislocation creep at T = 573, 673, and 773 K, respectively (Section IV–A). The three principal deformation mechanisms, operative in the fine-grained materials, are indicated in (d). (*a*) Alloy AlC0R (coarse grain), (*b*) alloy AlC0 (fine grain), (*c*) alloy AlC1 (fine grain), (*d*) alloy AlC2 (fine grain) (the data point marked by arrow has been obtained after prior creep deformation at $\dot{\varepsilon}/D_v = 2.3 \cdot 10^6$ m^{-2} and T = 773 K), and (*e*) alloy AlMg4C1 (fine grain).

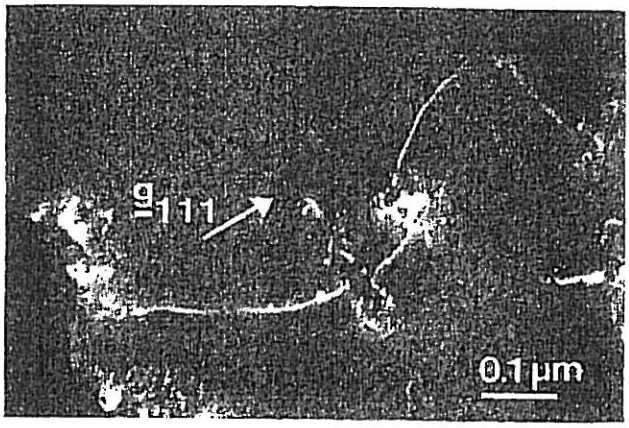

(*a*)

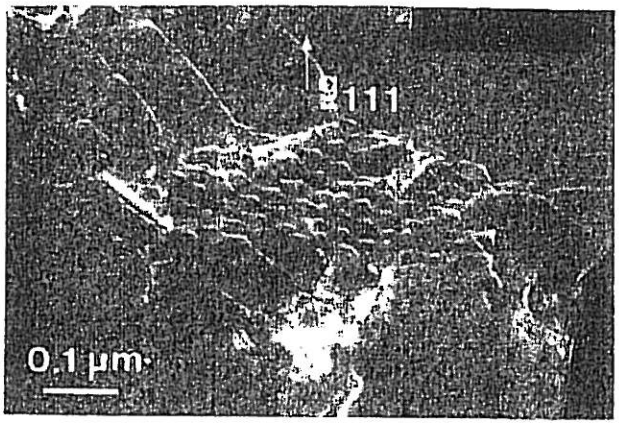

(*b*)

Fig. 13—Characteristic dislocation configurations after creep deformation: (*a*) Interaction of single dislocations with dispersoid particles in the regime of high stress exponent n (material: AlC2, T = 773 K, $\dot{\varepsilon}/D_v = 1.7 \cdot 10^8$ m^{-2}) and (*b*) formation of dislocation networks at high strain rates (material AlC2, T = 573 K, $\dot{\varepsilon}/D_v = 2.9 \cdot 10^{13}$ m^{-2}).

strain of both materials increases with $\dot{\varepsilon}$ from less than 1 pct to more than 10 pct (AlC0). Typical fracture surfaces obtained at small and large strain rates are represented in Figure 16 for the fine-grained material. Apparent is a transition from brittle fracture, oriented perpendicular to the stress axis, to ductile fracture with increasing strain rate. At $\dot{\varepsilon} > 10^{-7}$ s^{-1}, ductile fracture prevails over the entire cross section (Figure 15). Detailed views of the brittle fracture surface indicate intergranular failure (Figure 17). Individual grains can be identified at the bottom of the shallow dimples, with their sizes corresponding well to the actual grain diameters of 1.9 and 0.7 μm for materials AlC0 and AlC2, respectively.

Fracture surfaces of the coarse-grained material AlC0R exhibit the same features (Figure 18). However, fracture is transcrystalline, as can be seen from a longitudinal section through a brittle fracture surface (Figure 19). No pullout of the interlocked grains is observed. The transition strain rate (100 pct ductile failure) was found to be $\dot{\varepsilon} \approx 10^{-6}$ s^{-1} (Figure 15).

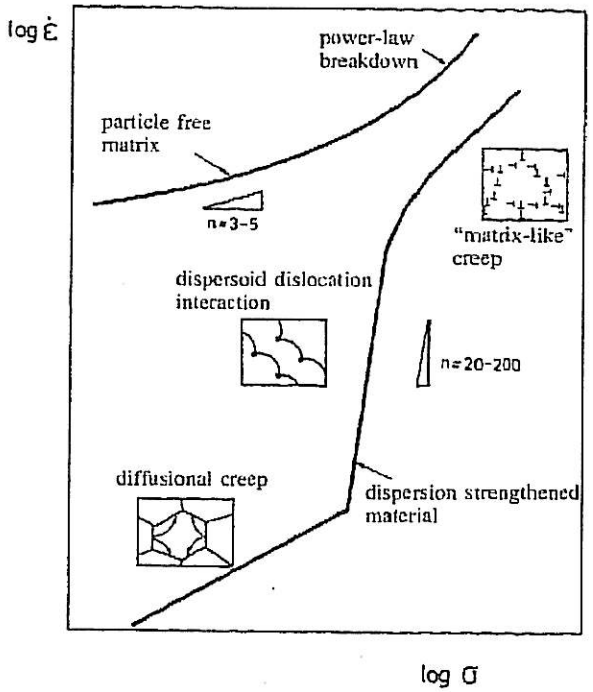

Fig. 14—Schematic comparison between the creep behavior of dispersion-strengthened and particle-free aluminum. Different deformation mechanisms, operative in dispersion-strengthened aluminum, are indicated.

IV. DISCUSSION

The experimental results reported above suggest that the high-temperature creep strength is controlled, first, by the strengthening contribution of the dispersoid particles (giving rise to a region of high stress exponent) and, second, by the grain morphology which can adversely affect the high strength obtained through dispersion hardening. In the following sections, we will examine both effects consecutively and will address the question of how dispersion-strengthened aluminum may be optimized with respect to dispersoid parameters and grain morphology. Finally, we will discuss the fracture behavior observed in these materials.

A. *The Strengthening Effect of Dispersoid Particles at High Temperatures*

All materials investigated exhibit a region of extremely high stress sensitivity. This behavior is unique for dispersion-hardened materials and must therefore be attributed to the interaction between moving dislocations and dispersoid particles. The first theory which provided a possible rationalization of this behavior was that of "local climb" proposed by Brown and Ham[27] and Shewfelt and Brown.[28] As a consequence of the particular climb geometry assumed in this model, a threshold stress $\sigma_{th}^{l} = 0.4$ to $0.7 \cdot \sigma_O$ was predicted, below which creep should be negligible. Although successful in explaining high stress exponents, the "local climb" model hinges on the assumption of a highly unstable dislocation geometry.[29,30] Under more realistic assumptions, it turns out

Table VIII. Compilation of Tensile Creep Data for Investigated Materials*

Material	T (K)	σ (MPa)	$\sigma/E \cdot 10^3$	$\dot{\varepsilon}$ (s^{-1})	$\dot{\varepsilon}/D_v$ (m^{-2})	ε_f [Pct]	t_f (s)	A_d [Pct]
AlC0	773	34.6	0.692	$7.4 \cdot 10^{-4}$	$1.71 \cdot 10^{10}$	11.60	59	100
		31.8	0.636	$1.7 \cdot 10^{-4}$	$3.94 \cdot 10^{9}$	10.70	126	100
		29	0.580	$9.5 \cdot 10^{-7}$	$2.20 \cdot 10^{7}$	2.53	3780	100
		26	0.520	$6.7 \cdot 10^{-7}$	$1.55 \cdot 10^{7}$	4.30	4440	100
		29.5	0.590	$1.1 \cdot 10^{-7}$	$2.55 \cdot 10^{6}$	—	—	—
		23	0.460	$6.9 \cdot 10^{-8}$	$1.60 \cdot 10^{6}$	—	—	—
		24	0.480	$5.6 \cdot 10^{-8}$	$1.30 \cdot 10^{6}$	—	—	—
		19	0.380	$4.2 \cdot 10^{-8}$	$9.74 \cdot 10^{5}$	0.61	$5.36 \cdot 10^{4}$	75
		24	0.480	$2.8 \cdot 10^{-8}$	$6.50 \cdot 10^{5}$	—	—	—
		22	0.440	$2.3 \cdot 10^{-8}$	$5.34 \cdot 10^{5}$	—	—	—
		23	0.460	$1.98 \cdot 10^{-8}$	$4.59 \cdot 10^{5}$	—	—	—
		22	0.440	$1.8 \cdot 10^{-8}$	$4.18 \cdot 10^{5}$	0.92	$7.92 \cdot 10^{4}$	52
		20.5	0.410	$1.4 \cdot 10^{-8}$	$3.25 \cdot 10^{5}$	—	—	—
		20	0.400	$1.3 \cdot 10^{-8}$	$3.02 \cdot 10^{5}$	—	—	—
		17.9	0.358	$1.1 \cdot 10^{-8}$	$2.55 \cdot 10^{5}$	—	—	—
		22	0.440	$8.8 \cdot 10^{-9}$	$2.04 \cdot 10^{5}$	0.88	$2.18 \cdot 10^{5}$	41
		17.5	0.350	$7.5 \cdot 10^{-10}$	$1.74 \cdot 10^{4}$	—	—	—
		19	0.380	$4.4 \cdot 10^{-10}$	$1.02 \cdot 10^{4}$	0.81	$2.18 \cdot 10^{6}$	36
		19.5	0.390	$3 \cdot 10^{-10}$	$6.96 \cdot 10^{3}$	—	—	—
AlC0R	673	37.8	0.756	$1.9 \cdot 10^{-5}$	$1.17 \cdot 10^{10}$	—	—	—
		35.4	0.708	$9.5 \cdot 10^{-7}$	$5.86 \cdot 10^{8}$	—	—	—
		33.8	0.676	$3.6 \cdot 10^{-7}$	$2.22 \cdot 10^{8}$	—	—	—
		31.7	0.634	$7.1 \cdot 10^{-9}$	$4.38 \cdot 10^{6}$	—	—	—
	773	30.0	0.600	$1.7 \cdot 10^{-4}$	$3.94 \cdot 10^{9}$	4.43	87	100
		32.4	0.648	$1.5 \cdot 10^{-4}$	$3.48 \cdot 10^{9}$	2.47	110	—
		27.8	0.556	$2.7 \cdot 10^{-5}$	$6.26 \cdot 10^{8}$	4.95	594	100
		27.3	0.546	$2.4 \cdot 10^{-5}$	$5.57 \cdot 10^{8}$	4.47	780	100
		27.3	0.546	$8.6 \cdot 10^{-6}$	$2.00 \cdot 10^{8}$	2.42	810	100
		29.4	0.588	$7.6 \cdot 10^{-6}$	$1.76 \cdot 10^{8}$	2.64	1620	87
		30.7	0.614	$3.7 \cdot 10^{-6}$	$8.58 \cdot 10^{7}$	1.93	1860	—
		27.3	0.546	$7.0 \cdot 10^{-7}$	$1.62 \cdot 10^{7}$	0.98	4620	—
		28.0	0.560	$6.7 \cdot 10^{-7}$	$1.55 \cdot 10^{7}$	1.14	3840	88
		29.2	0.584	$3.3 \cdot 10^{-7}$	$7.66 \cdot 10^{6}$	1.16	8820	61
		26.1	0.522	$8.4 \cdot 10^{-8}$	$1.95 \cdot 10^{6}$	0.44	$1.99 \cdot 10^{4}$	—
		26.3	0.526	$7.4 \cdot 10^{-8}$	$1.71 \cdot 10^{6}$	0.48	$2.47 \cdot 10^{4}$	63
		27.1	0.542	$3.3 \cdot 10^{-8}$	$7.66 \cdot 10^{5}$	0.48	$3.50 \cdot 10^{4}$	51
		26.5	0.530	$1.1 \cdot 10^{-8}$	$2.55 \cdot 10^{5}$	—	—	55
		26.4	0.528	$3.6 \cdot 10^{-9}$	$8.35 \cdot 10^{4}$	0.20	$9.86 \cdot 10^{4}$	45
		26.8	0.536	$2.1 \cdot 10^{-9}$	$4.87 \cdot 10^{4}$	—	—	—

*$\dot{\varepsilon}$, steady-state creep rate; ε_f, strain at failure; t_f, rupture time; and A_d, area fraction of ductile failure.

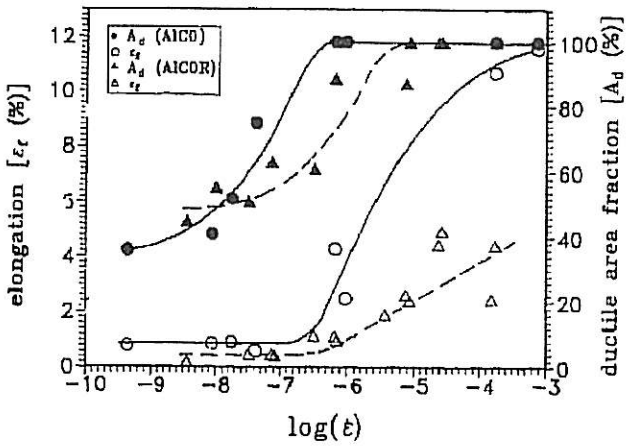

Fig. 15—Plot of strain to failure ε_f and area fraction A_d of the ductile failure mode *vs* strain rate $\dot{\varepsilon}$ for materials AlC0 and AlC0R (T = 773 K).

that climb of dislocations over particles of low volume fraction is rapid[30] and that threshold stresses are far too small to account for the high stress exponents of dispersion-hardened materials.[30,31]

Because of this inadequacy of the "local climb" theory, attention has recently been focused on dislocation detachment from the dispersoid particles as the likely rate-controlling mechanism.[11,32–35] Based on an analysis by Arzt and Wilkinson[34] of the detachment energetics, Rösler[11] and Rösler and Arzt[35] derived a new constitutive equation for dispersion-strengthened materials. They showed that when the detachment process is rate controlling, the stress-strain rate dependence is given by

$$\dot{\varepsilon} = \dot{\varepsilon}_0 \cdot \exp\left(-\frac{G\mathbf{b}^2 r[(1-k)\cdot(1-\sigma/\sigma_d)]^{3/2}}{k_B T}\right) \quad [2]$$

with

$$\dot{\varepsilon}_0 = 6\lambda\rho D_v/\mathbf{b} \quad [3]$$

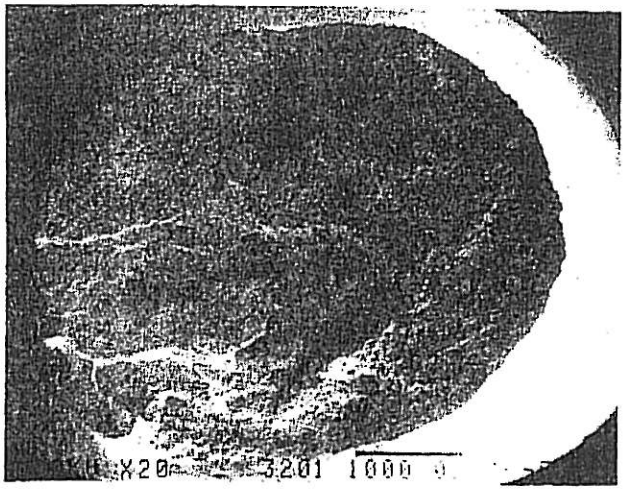

(*a*)

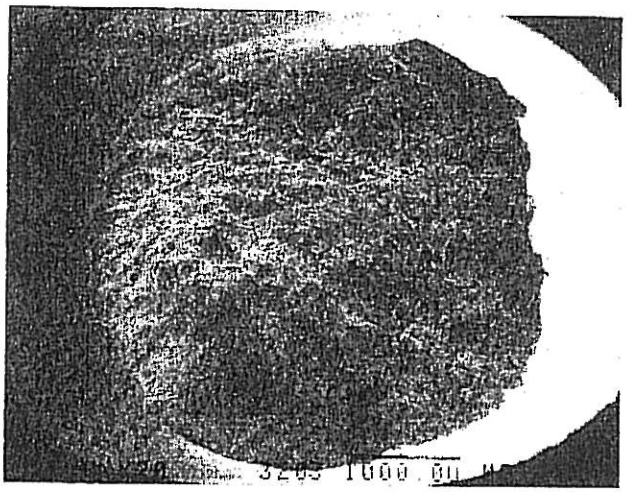

(*b*)

Fig. 16—Fracture surfaces of material AlC0 after creep deformation at (*a*) $\dot{\epsilon} = 8.8 \cdot 10^{-9}\ s^{-1}$ and (*b*) $\dot{\epsilon} = 6.7 \cdot 10^{-7}\ s^{-1}$, respectively.

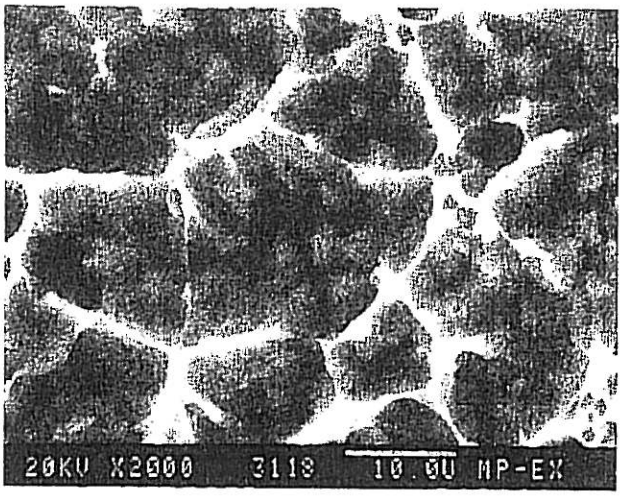

(*a*)

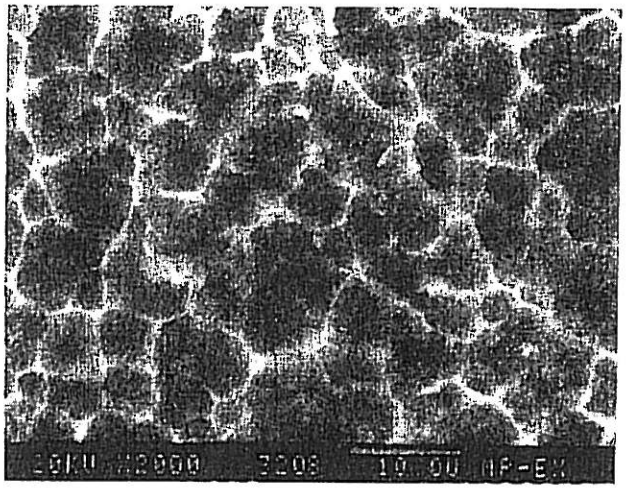

(*b*)

Fig. 17—Detailed view of the brittle fracture surface for (*a*) material AlC0 and (*b*) material AlC2. Individual grains can be identified at the bottom of the shallow dimples, indicating intercrystalline fracture.

Here, $k = T_P/T_M$ is the "relaxation factor" describing the ratio of the dislocation line energy T_p at the particle to that in the matrix (T_M), and $\sigma_d = \sigma_0 \cdot (1 - k^2)^{1/2}$ is the athermal detachment stress required for dislocation detachment in the absence of thermal activation.

As in other studies on dispersion-strengthened materials,[36,37,38] our TEM micrographs taken after creep deformation (Figure 20) suggest indeed that dislocations are captured at the departure side of the particles in dispersion-strengthened aluminum. Since the dislocation contrast disappears at the particles, it is difficult to assess on which side of the particle the dislocation is actually located. However, the disappearance of the dislocation contrast by itself points to considerable relaxation of line energy at the particle and, hence, to a strong detachment barrier.

The relaxation factor k is expected to be a unique quantity for a given matrix/dispersoid combination. It may, in principle, vary between 0 (complete relaxation,

Fig. 18—Fracture surfaces of material AlC0R after creep deformation at $\dot{\epsilon} = 1.1 \cdot 10^{-8}\ s^{-1}$.

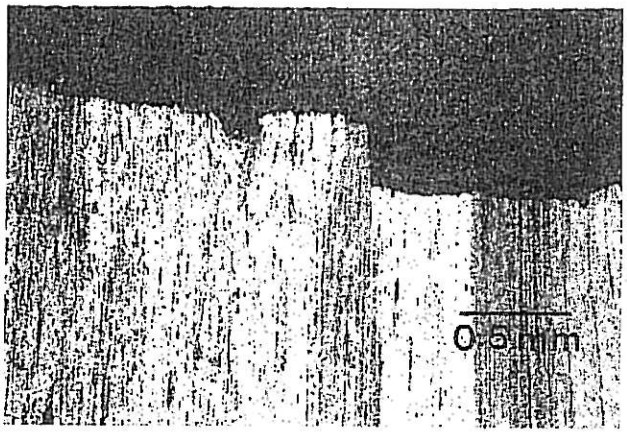

Fig. 19—Longitudinal section through the area of brittle fracture in Fig. 18. The planar crack front indicates transcrystalline failure. No pullout of the highly elongated grains is observed.

i.e., maximum interaction) and 1 (no relaxation, *i.e.*, no attractive interaction). Since its magnitude depends on the interfacial properties, the creep strength will vary for different matrix/dispersoid combinations at fixed particle size and volume fraction—a conclusion which is very different from predictions based on the "local climb" assumption. Which particle/matrix combination is chosen can therefore be of significant importance in high-temperature applications.

Inspection of Table VII and Figures 12(d) and (e) shows a remarkable feature: carbide dispersion-strengthened aluminum (AlC2) is significantly stronger at high temperatures than aluminum strengthened primarily by magnesium oxide (AlMg4C1), although alloy AlMg4C1 has a higher particle volume fraction and a smaller particle size (Table II, Section III–A–3). At $T = 673$ K and $\dot{\varepsilon}/D = 10^{10}$ m^{-2}, the creep strength advantage is about 20 pct. Oliver and Nix, who obtained similar results,[10] have proposed particle deformation as a possible cause for the inferiority of MgO-strengthened aluminum at high temperatures. However, particle deformation can only facilitate overcoming the climb barrier, while the detachment barrier, which in our interpretation is rate controlling, remains unchanged. It seems therefore likely that a stronger attractive force on dislocations accounts for the superior creep strength of carbide dispersion-strengthened aluminum.

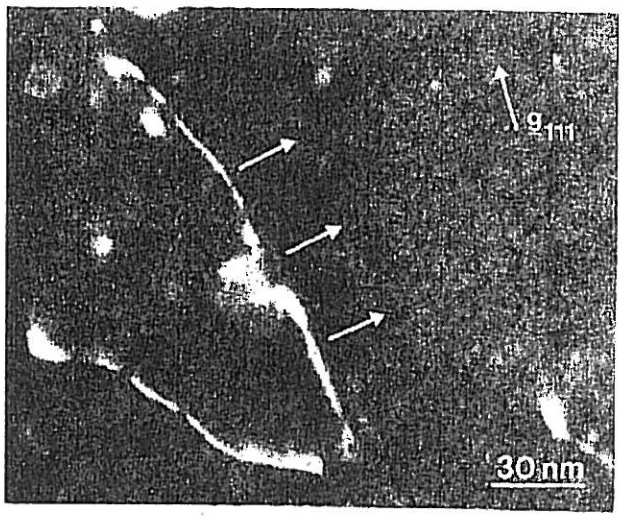

Fig. 20—Weak-beam image of a dislocation-particle-configuration after creep deformation (material AlC0), indicating detachment-controlled dislocation creep. Note that the dislocation contrast disappears at the dispersoid particles. Arrows indicate direction of dislocation motion.

More precise statements about the interaction strength can be drawn by determining the k factor from creep data.[11,35] Differentiation of Eq. [2] with respect to stress gives

$$k = 1 - \left(\frac{2k_B T}{3Gb^2 r} \cdot \frac{n_{app}}{(1 - \sigma/\sigma_d)^{1/2} \cdot \sigma/\sigma_d} \right)^{2/3} \qquad [4]$$

where r and $\sigma_O = \sigma_d \cdot \sqrt{1 - k^2}$ may be obtained from microstructural analysis (Section III–A–3) and/or measurement of the room-temperature yield strength (Table VI) and n_{app} is the measured (apparent) stress exponent. The important quantity determining the magnitude of k is n_{app}/r, since $(1 - \sigma/\sigma_d)^{1/2} \cdot \sigma/\sigma_d$ varies only slightly for $0.4 < \sigma/\sigma_d < 0.9$. Thus, a strong pinning force on moving dislocations is reflected in a high value of n_{app}/r.

Inspection of Figures 12(a) through (e) reveals that the stress exponent of materials AlC1 and AlC2 is indeed the highest, which is in accordance with the explanation given above for their superior creep properties. In the regime of particle-dislocation interaction controlled creep (Figures 12(d) and 14), the creep stress is virtually independent of the strain rate over several orders of magnitude. In fact, linear regression would reveal a negative slope for some data sets which is physically not meaningful. However, a slope of about 200 seems to represent the creep data fairly well, although it is obvious that with such high expectations, a power-law dependence can no longer be justified. In comparison, the stress exponent of materials AlC0, AlC0R, and AlMg4C1 is significantly smaller. From linear regression, one obtains $n_{app} \approx 72$ for AlC0R (compression creep data at 773 K), $n_{app} \approx 68$ for AlMg4C1 (compressive creep data at 673 K), and $n_{app} \approx 44$ for AlC0 (compression creep data at 673 K). Estimates for k obtained from Eq. [4] are $k \approx 0.79$, 0.80, 0.87, 0.75, and 0.74 for materials AlC0R, AlC0, AlMg4C1, AlC1, and AlC2, respectively.*

*Parameters used are n_{app} as given above, $r = \pi/4 \cdot d_p/2$ from Section III–A–3, and the temperature-corrected Orowan stress $\Delta\sigma_O$ from Table VI. The factor $\pi/4$ accounts approximately for the statistical distribution of the particle intersect height.[11,35] The stress σ inserted in Eq. [4] has to be that at which n_{app} is measured. Its choice is, however, uncritical because of the weak dependence of k on σ/σ_d. As typical values, we have inserted $\sigma = 31$ MPa (ALC0R), 40 MPa (AlC0), 83 MPa (AlMg4C1), 62 MPa (AlC1), and 100 MPa (AlC2).

Values obtained for k should be considered with caution, because considerable experimental uncertainties are connected with the determination of n_{app} and r. Also, it cannot be ruled out that concurrent grain boundary processes contribute to the deformation even in the regime of high stress exponent, which limits the applicability of Eq. [2]. Comparison of materials AlC0 (fine-grained) and AlC0R (coarse-grained) reveals, in fact, that the

pronounced temperature dependence observed for the fine crystalline materials is greatly reduced in the coarse-grained material, which points to contributions from grain boundaries. Fortunately, knowledge of the temperature dependence is not needed, and the determination of k from Eq. [4] seems therefore justified. This is also reflected in the nearly identical values of k obtained for AlC0 and AlC0R.

The theoretical stress-strain rate dependence according to Eq. [2] is compared in Figures 12(a) through (e) with the experimental data. Considering that the only free parameter of Eq. [2] is the relaxation factor k (r and σ_0 resulting from the microstructural examination and the Orowan stress estimate), a quite satisfactory agreement with the data of the coarse-grained material AlC0R is found. Naturally, the model is not capable of reflecting the transition in stress exponent at high and low strain rates nor the temperature dependence in the case of the fine crystalline materials, since it considers only dislocation detachment. Note, however, that a finite temperature dependence is predicted as a consequence of thermally activated detachment.

Although not fully quantitative, the values of k point to a certain trend: Carbides seem to be more efficient dispersoids in aluminum matrices than the oxides Al_2O_3 and MgO. In particular, MgO seems to be a relatively inefficient barrier for dislocation motion at high temperatures. Hence, magnesium appears to be an inadequate alloying element in dispersion-strengthened aluminum alloys for high-temperature applications, unless oxygen pickup is greatly reduced during fabrication. On the other hand, Al_4C_3 seems to have desirable properties. The low value of k, which is reflected in the extremely high stress exponent, is exceptional also compared to other material classes, such as dispersion-hardened nickel-base superalloys.[11,35]

B. *The Effect of Grain Size on the High-Temperature Strength*

At low strain rates ($\dot{\varepsilon}/D < 70^6$ to 10^8 m^{-2}), the stress exponent changes rapidly from extremely high values to $n \approx 13$ in the case of the fine-grained materials.* The transition to lower stress intensities at low strain rates could be interpreted as a degradation of creep strength, indicative of microstructural instability in the form of dynamic recrystallization and grain or particle coarsening. These possibilities can, however, be ruled out, because on reloading of specimens crept at the lowest strain rates, the strength at higher strain rates was fully recoverable (Figure 12(d)). In addition, no measurable increase in grain size or particle diameter was observed after creep deformation. Also, the fact that material AlC0R shows stable creep behavior with high stress sensitivity at $\dot{\varepsilon}/D < 10^7$ m^{-2} points to high thermal stability of the dispersoid particles.

Alternatively, the transition in stress exponent can be attributed to diffusional creep. The stress exponent lies, however, between $n = 1$, which would be expected from classical diffusional creep theory,[39,40] and that for dislocation creep. Matsuda and Matsuura[41] suggested a coupling between grain boundary sliding and dislocation creep as a possible cause. However, the fact that $n \approx 13$ prevails over many orders in magnitude of $\dot{\varepsilon}$ (Figure 12(b)) seems to be inconsistent with that explanation. It has been demonstrated by finite element calculations that, except in a narrow transition region, the stress exponent is still determined by that of dislocation creep when such a coupling takes place.[42]

A second model capable of explaining anomalously high stress exponents is that of interface-reaction controlled diffusional creep.[43,44] It assumes that vacancy generation and annihilation require the motion of grain boundary dislocations which have to bypass dispersoid particles in the grain boundary. Assuming that this bypass process is, like in the bulk material, controlled by thermally activated dislocation detachment, a rate equation can be derived (details will be published elsewhere[45]):

$$\dot{\varepsilon}_{\text{Diff}} = \frac{4\lambda\rho^e_{gb}D_v}{d_g \mathbf{b}_{gb}} \cdot \exp\left(-\frac{G\mathbf{b}^2_{gb}r[(1-k)(1-\sigma/\sigma_d)]^{3/2}}{k_BT}\right) \quad [5]$$

(ρ^e_{gb} is density of grain boundary edge dislocations) where $\mathbf{b}_{bg} \approx 0.5$ to $0.3\mathbf{b}$ is a typical estimate for the Burgers vector of a grain boundary dislocation.[43] Note that the stress exponent $n = \partial \log(\dot{\varepsilon})/\partial \log(\sigma)$ is predicted to scale with the square of the Burgers vector for both detachment-controlled diffusional creep (Eq. [5]) and detachment-controlled dislocation creep (Eq. [2]). Thus, when the rate-controlling mechanism changes accordingly, the stress exponent should be reduced by $(\mathbf{b}_{gb}/\mathbf{b})^2 \approx 1/4$ to $1/9$. This provides a possible explanation for the existence of an intermediate stress exponent.

As demonstrated in Figure 22, good agreement between the transverse creep data of material AlC0 and Eq. [5] is indeed found when physically reasonable values for $\mathbf{b}_{gb}$ and for the particle volume fraction at the grain boundaries are assumed. It is, however, surprising at first sight that, compared to transverse loading, $\dot{\varepsilon}_{\text{Diff}}$ is reduced by approximately five orders of magnitude under longitudinal loading, whereas the stress exponent remains the same. Very likely, the extremely strong [111] texture (Section III–A–2) plays an important role here. Under longitudinal loading, grain boundaries oriented perpendicular to the stress axis are almost entirely twist boundaries consisting mainly of screw dislocations. Hence, the density of edge dislocations, which are the sources and sinks for vacancies, is greatly diminished on transverse boundaries. A reduction in creep rate by five orders of magnitude requires a reduction of ρ^e_{gb} by the same amount which, in view of the sharp texture, is imaginable.

Although $\mathbf{b}_{gb}$ and the particle volume fraction at the grain boundaries are fit parameters to a large extent, it is encouraging that the observed creep behavior can be consistently interpreted under physically reasonable assumptions. In addition, if the proposed model proves to be correct, it becomes understandable why dispersion-strengthened aluminum is less prone to diffusional creep

*Although such a transition was not observed for material AlC1, it is anticipated that measurements at lower normalized strain rates $\dot{\varepsilon}/D$ would reveal the same behavior.

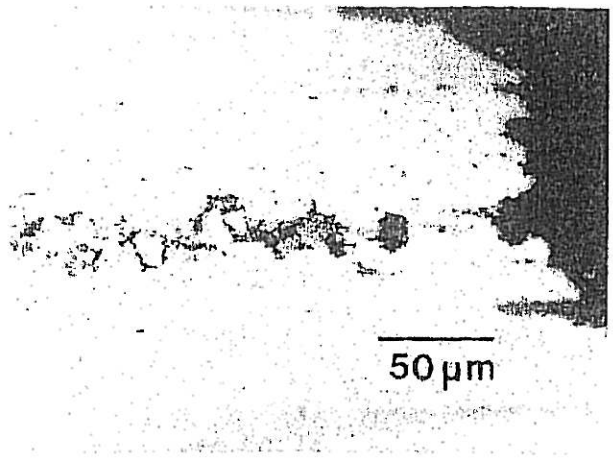

Fig. 21—Longitudinal section through fractured specimen. Creep damage along stringer of inclusions is evident.

than many other dispersion-strengthened materials, such as fine-grained, texture-free nickel-base superalloys,[44,46] which even exhibit superplastic behavior. Very likely it is (1) the enrichment of dispersoid particles at the grain boundaries and/or (2) the strong texture which suppress diffusional creep. This might outline possibilities for the future design of materials with excellent high-temperature strength despite their fine-grained structure. Another case in point is TD-Ni and other similar alloys as studied by Wilcox and Clauer,[47] some of which have a grain structure similar to the alloys investigated here (fine, elongated, and textured grains) and do exhibit stress exponents significantly larger than one.

Whereas the generation of a coarse, elongated grain structure is instrumental for most nickel-base superalloys, it is of limited use for dispersion-strengthened aluminum because of these special features. A noticeable strength enhancement is only found at the most extreme temperatures and strain rates. On the other hand, some loss in room-temperature strength results from the lack of Hall-Petch hardening and the less favorable Taylor factor in extrusion direction.

C. *High-Temperature Fracture*

Because of the excellent high-temperature strength of dispersion-strengthened aluminum, a possible limitation for elevated temperature applications lies in the low strain to failure at strain rates which are typical of practical applications. Hereby, it is noteworthy that (1) ε_f can be small even though the area fraction of the ductile failure mode is considerable (Figure 15) and (2) the onset of enhanced ductility coincides with the complete disappearance of the brittle failure mode (Figure 15). These results indicate that deformation is strongly localized at small strain rates and that creep damage plays a dominant role in concentrating plastic deformation. Only if lifetimes are sufficiently short to completely prevent creep damage (*i.e.*, the brittle failure mode) is ε_f large.

Stringers of inclusions have frequently been identified as nucleation sites for creep damage (Figure 21). Closer examination reveals that the chemical composition of these stringers is identical with the matrix composition, except for a significantly higher oxygen content. Thus, it seems that these "inclusions" are, in fact, prior aluminum powder particles which have picked up a high dispersoid content during milling. Avoidance of such failure sites appears to be essential in order to further improve the high-temperature ductility. It should, however, be noted that limited failure strains due to localized plastic deformation are a drawback inherently associated with dispersion-strengthened materials. Although individual dispersoids may be too small to be considered as efficient failure sites, they do limit ductility by causing a high creep exponent n. Noting the difference in stress exponent between AlC0R and AlC0, it is consistent with the above interpretation that the fine-grained material exhibits larger fracture strains. The contribution of diffusional creep seems to make the material more tolerant against stress concentrations, overcompensating the effect of enhanced creep damage along grain boundaries. The qualification is, however, in order that some effect may also be due to the different specimen geometries (Section II–B). Generally, thicker and/or shorter samples, as used for AlC0, will exhibit larger failure strains when localized deformation occurs.

V. SUMMARY

1. The microstructure of aluminum alloys strengthened by oxide and carbide dispersoids was investigated with respect to grain morphology, texture, and particle structure. The dispersoid particles have been identified as γ- (or η-) Al_2O_3, Al_4C_3, and MgO.
2. The mechanical behavior at high temperatures was examined and correlated with the microstructural

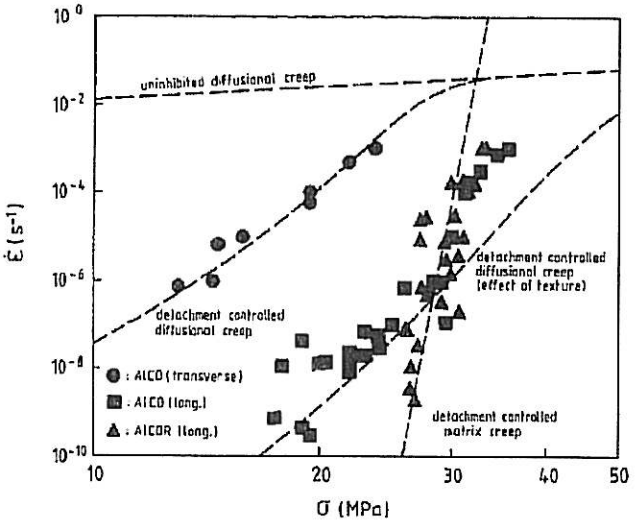

Fig. 22—Comparison between model equation [5] for detachment-controlled diffusional creep and experimental creep data of material AlC0 (T = 773 K). Best correlation is obtained for $\mathbf{b}_{sb} = 0.45 \cdot \mathbf{b}$ and $f_v^{sb} = 10 \cdot f_v$. In view of the significant particle enrichment at the grain boundaries (Fig. 2(b)), $f_v^{sb} \approx 19$ pct seems to be a reasonable assumption. The effect of texture was taken into account by assuming $\rho_{sb}^r \approx 10^{-5}\ \sigma/G\mathbf{b}$ instead of $\rho_{sb}^r \approx \sigma/G\mathbf{b}$ (Section IV–B). The relaxation factor k was assumed to be the same as obtained for matrix dislocations (Section IV–A).

properties. New theoretical concepts have been used to analyze the strengthening effect of different dispersoid types. It was concluded that aluminum carbide impedes dislocation creep more effectively than the oxide particles (Al_2O_3, MgO) and seems therefore more suitable for high-temperature applications.

3. Compared to other fine-grained materials, dispersion-strengthened aluminum is, in its fine crystalline condition, remarkably resistant against diffusional creep. It is suggested that this behavior is due to a unique combination of a strong ⟨111⟩ fiber texture with a high dispersoid concentration at the grain boundaries. A noticeable strength advantage of the recrystallized material was only found at $T = 773$ K. Therefore, costly thermomechanical treatment may be avoidable for most applications, especially since lack of Hall-Petch hardening and texture weakening lead to a reduced room-temperature tensile strength in the coarse-grained condition.
4. High-temperature fracture was investigated. Stress localization due to creep damage, combined with the high stress exponent of dispersion-strengthened materials, limits the macroscopic strain to failure. This is inevitably the price which has to be payed for the high strength caused by a strong particle-dislocation interaction.

ACKNOWLEDGMENTS

The authors would like to thank Dr. Hartig and Professor Mecking (Technical University of Hamburg-Harburg, Federal Republic of Germany) for performing the texture analysis. The research leading to this article has been supported financially by the Bundesministerium für Forschung und Technologie under Project No. 03 M0010 E4.

REFERENCES

1. R. Irmann: *Tech. Rundsch.*, 1949, vol. 41, pp. 19-20.
2. A. von Zeerleder: *Z. Metallkd.*, 1950, vol. 41, pp. 228-31.
3. E.A. Bloch: *Met. Rev.*, 1961, vol. 6, pp. 193-239.
4. F.V. Lenel, G.S. Ansell, and E.C. Nelson: *Trans. AIME*, 1957, vol. 209, pp. 117-21.
5. J.S. Benjamin and M.J. Bomford: *Metall. Trans. A*, 1977, vol. 8, pp. 1301-05.
6. G. Jangg, F. Kutner, and G. Korb: *Aluminum*, 1975, vol. 51, pp. 641-45.
7. G. Jangg, F. Kutner, and G. Korb: *Powder Metall. Int.*, 1977, vol. 9, pp. 24-26.
8. V. Arnold and J. Baumgarten: *Powder Metall. Aerospace Mater.*, 1984, vol. 1, pp. 1-20.
9. K. Kucherova, A. Orlova, H. Oikawa, and J. Cadek: *Mater. Sci. Eng. A*, 1988, vol. 102, pp. 201-09.
10. W.C. Oliver and W.D. Nix: *Acta Metall.*, 1982, vol. 30, pp. 1335-47.
11. J. Rösler: *VDI Fortschr.-Ber.*, VDI-Verlag, Düsseldorf, 1988, vol. 5 (154), pp. 1-200.
12. R. Joos: Diploma Thesis, University of Stuttgart, Federal Republic of Germany, 1988.
13. L.J. Barker: *Trans. ASM*, 1949, vol. 42, pp. 347-51.
14. C. Zener as quoted by C.S. Smith: *Trans. AIME*, 1948, vol. 175, pp. 15-18.
15. R.F. Singer, W.C. Oliver, and W.D. Nix: *Metall. Trans. A*, 1980, vol. 11, pp. 1895-1901.
16. M. Slesar, M. Besterci, G. Jangg, M. Miskovicova, and K. Pelikan: *Z. Metallkd.*, 1988, vol. 79, pp. 56-63.
17. D. Altenpohl: *Aluminum und Aluminumlegierungen*, Springer-Verlag, Berlin, 1965, pp. 395-96.
18. Y.W. Kim, W.M. Griffith, and F.H. Froes: *J. Met.*, 1985, pp. 27-33.
19. G. Staniek: *Aluminum*, 1984, vol. 60, pp. 923-29.
20. G. Hass: *Z. Anorg. Chem.*, 1947, vol. 254, pp. 96-106.
21. N.A. McKinnon: Report SM205, Aeronautical Research Laboratories, Melbourne, Australia, 1953.
22. *Alumina as a Ceramic Material*, W.H. Gitzen, ed., The American Ceramic Society, Inc., Columbus, OH, 1970, pp. 14-35.
23. W. Kleber: *Einführung in die Kristallographie*, VEB Verlag Technik, Berlin, 1958, p. 176.
24. M. von Stackelberg and E. Schnorrenberg: *Z. Phys. Chem. B*, 1934, vol. 27, pp. 37-49.
25. J.-J. Valencia, C. McCullough, J. Rösler, C.G. Levi, and R. Mehrabian: in *Solidification of Metal Matrix Composites*, P. Rohatgi, ed., TMS, Warrendale, PA, 1990, pp. 133-50.
26. N. Hansen: *Trans. TMS-AIME*, 1969, vol. 245, pp. 1305-12.
27. L.M. Brown and R.K. Ham: in *Strengthening Methods in Crystals*, A. Kelly and R.B. Nicholson, eds., Elsevier, Amsterdam, 1971, pp. 10-134.
28. R.S.W. Shewfelt and L.M. Brown: *Phil. Mag.*, 1977, vol. 35, pp. 945-62.
29. R. Lagneborg: *Scripta Metall.*, 1973, vol. 7, pp. 605-13.
30. J. Rösler and E. Arzt: *Acta Metall.*, 1988, vol. 36, pp. 1043-51.
31. W. Blum and B. Reppich: in *Creep Behavior of Crystalline Solids*, B. Wilshire and R.W. Evans, eds., Pineridge Press, Swansea, United Kingdom, 1985, pp. 83-135.
32. D.J. Srolovitz, R.A. Petkovic-Luton, and M.J. Luton: *Acta Metall.*, 1983, vol. 31, pp. 2151-59.
33. D.J. Srolovitz, M.J. Luton, R.A. Petkovic-Luton, D.M. Barnett, and W.D. Nix: *Acta Metall.*, 1984, vol. 32, pp. 1079-88.
34. E. Arzt and D.S. Wilkinson: *Acta Metall.*, 1986, vol. 34, pp. 1893-98.
35. J. Rösler and E. Arzt: *Acta Metall. Mater.*, 1990, vol. 38, pp. 671-83.
36. V.C. Nardone and J.K. Tien: *Scripta Metall.*, 1983, vol. 17, pp. 467-72.
37. J.H. Schröder and E. Arzt: *Scripta Metall.*, 1985, vol. 19, pp. 1129-34.
38. R.S. Herrick, J.R. Weertman, R. Petkovic-Luton, and M.J. Luton: *Scripta Metall.*, 1988, vol. 22, pp. 1879-84.
39. C. Herring: *J. Appl. Phys.*, 1950, vol. 21, pp. 437-45.
40. R.L. Coble: *J. Appl. Phys.*, 1963, vol. 34, pp. 1679-84.
41. N. Matsuda and K. Matsuura: *Trans. Jpn. Inst. Met.*, 1953, vol. 28, pp. 392-405.
42. F.W. Crossman and M.F. Ashby: *Acta Metall.*, 1975, vol. 23, pp. 425-40.
43. E. Arzt, M.F. Ashby, and R.A. Verall: *Acta Metall.*, 1983, vol. 31, pp. 1977-89.
44. R. Timmins and E. Arzt: in *Structural Applications of Mechanical Alloying*, F.H. Froes and J.J. de Barbadillo, eds., ASM INTERNATIONAL, Metals Park, OH, 1990, pp. 67-77.
45. J. Rösler: Max-Planck-Institut für Metallforschung, Stuttgart, Germany, unpublished research, 1990.
46. J.K. Gregory, J.C. Gibeling, and W.D. Nix: *Metall. Trans. A*, 1985, vol. 16, pp. 777-87.
47. B.A. Wilcox and A.H. Clauer: *Acta Metall.*, 1972, vol. 20, pp. 743-57.
48. *CRC Handbook of Chemistry and Physics*, 65th ed., R.C. Weast, ed., CRC Press Inc., Boca Raton, FL, 1984, p. B-111.
49. W. Köster: *Z. Metallkd.*, 1948, vol. 39, pp. 1-9.
50. H.J. Frost and M.F. Ashby: *Deformation Mechanism Maps*, Pergamon Press, Oxford, United Kingdom, 1982, pp. 20-29.